

## ATMOSPHERIC CIRCULATION OF HOT JUPITERS: THREE-DIMENSIONAL CIRCULATION MODELS OF HD 209458b AND HD 189733b WITH SIMPLIFIED FORCING

ADAM P. SHOWMAN,<sup>1</sup> CURTIS S. COOPER,<sup>1,2</sup> JONATHAN J. FORTNEY,<sup>3,4,5</sup> AND MARK S. MARLEY<sup>5</sup>

Received 2008 January 13; accepted 2008 April 10

### ABSTRACT

We present global, three-dimensional numerical simulations of the atmospheric circulation on HD 209458b and HD 189733b and calculate the infrared spectra and light curves predicted by these simulations, which we compare with available observations. Radiative heating/cooling is parameterized with a simplified Newtonian relaxation scheme. Our simulations develop day-night temperature contrasts that vary strongly with pressure. At low pressure ( $<10$  mbar), air flows from the substellar point toward the antistellar point, both along the equator and over the poles. At deeper levels, the flow develops an eastward equatorial jet with speeds of  $3\text{--}4\text{ km s}^{-1}$ , with weaker westward flows at high latitudes. This basic flow pattern is robust to variations in model resolution, gravity, radiative time constant, and initial temperature structure. Nightside spectra show deep absorption bands of  $\text{H}_2\text{O}$ ,  $\text{CO}$ , and/or  $\text{CH}_4$ , whereas on the dayside these absorption bands flatten out or even flip into emission. This results from the strong effect of dynamics on the vertical temperature-pressure structure; the temperature decreases strongly with altitude on the nightside but becomes almost isothermal on the dayside. In *Spitzer* bandpasses, our predicted planet-to-star flux ratios vary by a factor of  $\sim 2\text{--}10$  with orbital phase, depending on the wavelength and chemistry. For HD 189733b, where a detailed  $8\text{ }\mu\text{m}$  light curve has been obtained, we correctly produce the observed phase offset of the flux maximum, but we do not explain the flux minimum and we overpredict the total flux variation. This discrepancy likely results from the simplifications inherent in the Newtonian relaxation scheme and provides motivation for incorporating realistic radiative transfer in future studies.

*Subject headings:* atmospheric effects — methods: numerical — planets and satellites: general — planets and satellites: individual (HD 209458b)

### 1. INTRODUCTION

Of the  $\sim 277$  extrasolar giant planets (EGPs) that have been discovered to date,<sup>6</sup> the hot Jupiters have proved the easiest to characterize because of their high temperatures, short orbital periods, and likelihood of transiting their stars (Charbonneau et al. 2007). The planetary mass and radius can be calculated from radial velocity and transit data, allowing the surface gravity to be inferred; furthermore, the rapid spin-down times for such close-in planets (Guillot et al. 1996) suggest that these planets are tidally locked, providing an estimate of their rotation rates. Such tidal locking implies that, in the absence of atmospheric winds, the dayside would be extremely hot and the nightside would be extremely cold.

Impressively, infrared light curves have been obtained with the *Spitzer Space Telescope* for at least six hot Jupiters, helping to constrain the three-dimensional (3D) temperature pattern and atmospheric circulation of these objects. Continuous  $8\text{ }\mu\text{m}$  observations of HD 189733b over half an orbit demonstrate that the planet's photospheric temperatures are relatively homogenized: the nightside is perhaps only  $\sim 200\text{--}300\text{ K}$  colder than the dayside (Knutson et al. 2007). The exquisite temporal resolution allows detailed structure to be inferred. The light curve shows that the flux peaked  $16^\circ \pm 6^\circ$  of orbital phase before secondary eclipse; a flux map of the planet constructed from the light curve suggests that the hottest region lies  $\sim 30^\circ$  longitude east of the substellar

point and the coldest region lies a comparable amount west of the antistellar point, providing clear evidence for advection by winds (Knutson et al. 2007). Light curves at  $8\text{ }\mu\text{m}$  for HD 209458b and 51 Peg b have also been obtained (Cowan et al. 2007) and similarly imply significant thermal homogenization by winds, although these light curves contain insufficient temporal sampling to determine displacements (if any) of the hottest and coldest regions from the substellar and antistellar points. In contrast, Upsilon And b and HD 179949 exhibit large-amplitude phase variations, with no observationally significant phase shift, which suggests that these planets have large day-night temperature differences (perhaps  $>500\text{ K}$ ) that track the stellar insolation patterns (Harrington et al. 2006; Cowan et al. 2007). Together, these observations suggest that the degree to which winds homogenize the temperatures varies from planet to planet.

There exist many additional observational constraints on the circulation, including dayside spectra, upper limits on albedo, and constraints on composition. For HD 209458b, *Spitzer* secondary-eclipse photometry at wavelengths of  $3.6\text{--}24\text{ }\mu\text{m}$  suggests the existence of a hot stratosphere on the dayside (Knutson et al. 2008; Burrows et al. 2007b), while HD 189733b seems to lack such a temperature inversion. *Spitzer* IRS spectra of these planets' daysides from  $7\text{--}14\text{ }\mu\text{m}$  lack obvious molecular absorption bands (Grillmair et al. 2007; Richardson et al. 2003, 2007; Swain et al. 2008), although debate exists about the interpretation (Fortney & Marley 2007). Transit spectroscopy observations have yielded detections of sodium (Charbonneau et al. 2002; Redfield et al. 2008) and water (Barman 2007; Tinetti et al. 2007) on both planets, and upper limits on several other compounds.

Several groups have investigated the atmospheric circulation on hot Jupiters (for a review of the approaches see Showman et al. 2007). Cho et al. (2003, 2008) and Langton & Laughlin (2007, 2008) solved variants of the two-dimensional (2D) or quasi-2D

<sup>1</sup> Department of Planetary Sciences and Lunar and Planetary Laboratory, University of Arizona, 1629 University Boulevard, Tucson, AZ 85721; showman@lpl.arizona.edu.

<sup>2</sup> NASA Astrobiology Institute, University of Arizona, Tucson, AZ 85721.

<sup>3</sup> UCO/Lick Observatory, Department of Astronomy and Astrophysics, University of California, Santa Cruz, CA 95064.

<sup>4</sup> *Spitzer* Fellow.

<sup>5</sup> NASA Ames Research Center 245-3, Moffett Field, CA.

<sup>6</sup> See <http://www.exoplanet.eu>.

equations on a rotating sphere. The advantage of this approach is that, by reducing the vertical resolution to one layer, simulations with high horizontal resolution can be performed. The idealizations implicit in such simplified models also allow the model dynamics to be relatively easily understood; a comparison of such results with 3D models and observations can lend important insights into which dynamical processes cause which outcomes (Vasavada & Showman 2005; Showman et al. 2007). This has proved important, for example, in studying horizontal vortex/jet interactions on solar system giant planets and in Earth's stratosphere (Cho & Polvani 1996; Showman 2007; Polvani et al. 1995).

On the other hand, one-layer models do not represent the vertical structure of the flow, and they exclude inherently 3D processes such as baroclinic instabilities,<sup>7</sup> vortex tilting, and vertical wave propagation. In some contexts, such as the tropospheres of the Earth, Mars, Jupiter, and Saturn, 3D processes (e.g., baroclinic instabilities and convection) are crucial for determining the mean state because they convert potential energy to kinetic energy, hence causing the accelerations that pump the east-west jet streams. To some degree, such 3D processes can be parameterized in 2D models, but this introduces uncertainties regarding (for example) the rate at which the parameterized processes inject energy into the flow. In the hot-Jupiter context, a 3D approach is further motivated by the expectation that the radiative time constant varies by orders of magnitude in the vertical (Iro et al. 2005), which in the presence of the day-night heating gradient would cause patterns of temperature and wind that vary both vertically and horizontally in an inherently 3D manner. Because infrared spectra of planetary atmospheres depend sensitively on the vertical temperature profile, a full 3D representation of the winds and temperatures is also necessary for robustly predicting infrared spectra and wavelength-dependent light curves in *Spitzer* bandpasses.

In light of the above, we have adopted a 3D approach to investigate the atmospheric circulation of hot Jupiters (Cooper & Showman 2005, 2006; Showman & Guillot 2002). Cooper & Showman (2005, 2006) and Showman & Guillot (2002) focused on HD 209458b and approximated the dayside heating and nightside cooling using a Newtonian cooling/heating scheme, which parameterizes the radiative heating rate (in  $\text{K s}^{-1}$ ) as  $(T_{\text{eq}} - T)/\tau_{\text{rad}}$ , where  $T_{\text{eq}}$  is the specified radiative-equilibrium temperature profile (hot on the dayside, cold on the nightside),  $T$  is the actual temperature, and  $\tau_{\text{rad}}$  is the radiative-equilibrium timescale, which was taken to be a function of pressure. In Cooper & Showman (2005) the vertical structure of  $T_{\text{eq}}$  and  $\tau_{\text{rad}}$  were taken from Iro et al. (2005). The simulations showed development of several broad jets—including a superrotating<sup>8</sup> equatorial jet with speeds up to several  $\text{km s}^{-1}$ —and exhibited horizontal (day-night) temperature differences that varied strongly in height. Cooper & Showman (2006) extended these simulations to include carbon chemistry, which showed that interconversion between CO and  $\text{CH}_4$  should become chemically quenched at low pressure, leading to nearly constant abundances of these species everywhere above the photosphere at abundances that depend on the temperature in the deep ( $\sim 10$  bar) atmosphere. Using a multistream plane-parallel radiative-transfer code, Fortney et al. (2006a) calculated theoretical infrared light curves and spectra for HD 209458b from

<sup>7</sup> Baroclinic instabilities are a form of sloping convection that can occur in the presence of horizontal temperature contrasts in rotating, statically stable atmospheres. Lateral and vertical motion forces the cold air downward and the hot air upward, which releases potential energy that helps to drive the circulation. Most large-scale winter weather in the United States, Europe, and Asia is caused by baroclinic instabilities.

<sup>8</sup> Superrotation refers to eastward zonal winds, that is, winds moving faster than the planetary rotation.

the 3D temperature patterns of Cooper & Showman (2005, 2006). These calculations suggested that the day-night flux differences could reach factors of  $\sim 2$ – $10$  depending on wavelength and that the peak IR emission should lead the secondary eclipse by  $\sim 2$ – $3$  hr in most *Spitzer* IRAC bands.

Here, we present new global, 3D numerical simulations, spectra, and light curves that continue the research program begun by Cooper & Showman (2005, 2006) and Fortney et al. (2006a). Major improvements are incorporated in several areas. First, Cooper & Showman (2005, 2006) treated the day-night difference in  $T_{\text{eq}}$  as a free parameter (with values ranging from 100 to 1000 K) rather than the result of a laterally varying radiative-transfer calculation. This uncertainty in  $\Delta T_{\text{eq}}$  directly translates into uncertainty in the light curves and spectra. Within the context of the Newtonian-cooling framework, the best approach—which we take here—is to explicitly calculate the longitude, latitude, and height-dependent radiative-equilibrium temperatures for use in the Newtonian heating/cooling scheme.  $\Delta T_{\text{eq}}$  is thus no longer a free parameter but represents the true difference in radiative-equilibrium temperature from the dayside to the nightside. Likewise, we here calculate  $\tau_{\text{rad}}$  over the full 3D grid and express this as a function of *both* temperature and pressure rather than treating it as a function of *p* alone (based on the 1D global average temperature profile) as done by Cooper & Showman (2005, 2006).

Second, we consider not only HD 209458b (the canonical planet emphasized by most previous circulation studies) but HD 189733b, and perform parameter variations in planetary rotation rate, gravity, and radiative time constant to determine how these parameters affect the behavior. Finally, we calculate infrared spectra and light curves from the 3D temperature patterns for comparison with available observations, including the recent  $8 \mu\text{m}$  light curve for HD 189733b (Knutson et al. 2007), secondary-eclipse photometry for HD 189733b (Deming et al. 2006), and secondary-eclipse photometry for HD 209458b, which now spans all available *Spitzer* channels (Knutson et al. 2008; Deming et al. 2005).

A long-term goal is to couple the dynamics to a realistic representation of radiative transfer. However, this is a difficult task, and experience with planetary general circulation models (GCMs) shows that the radiative-transfer calculation can become a computational bottleneck, making such a model computationally expensive. The computational and conceptual simplicity of Newtonian cooling provide compelling arguments for documenting the extent to which a model driven by such simplified forcing can explain available observations. The results described herein thus provide a benchmark documenting the best that can be done with this simplified approach.

In § 2 we describe the dynamical model and present the calculations of laterally varying radiative-equilibrium temperature and radiative time constant. Section 3 presents the basic dynamical results and parameter variations. Section 4 describes the spectra and infrared light curves in *Spitzer* bandpasses as predicted by the simulations. Section 5 compares our results with pertinent aspects of dynamical calculations by other authors. Section 6 shows that the global-scale flow of hot Jupiters should be close to local hydrostatic balance, and § 7 concludes.

## 2. MODEL

### 2.1. Dynamics

We solve the global, three-dimensional primitive equations in spherical geometry using the ARIES/GEOS dynamical core (Suarez & Takacs 1995). The primitive equations are the standard equations for large-scale flow in stably stratified atmospheres whose horizontal dimensions greatly exceed the vertical dimensions. This is

expected to be true on hot Jupiters, which have horizontal scales of  $10^7$ – $10^8$  m but atmospheric scale heights of only 200–500 km, leading to a horizontal : vertical aspect ratio of  $\sim 20$ –500. This large aspect ratio allows the vertical momentum equation to be replaced with local hydrostatic balance, meaning that the local vertical pressure gradient  $\partial p/\partial z$  is balanced by the local fluid weight  $\rho g$  (for a derivation, see, e.g., Holton 2004). The primitive equations admit the full range of balanced motions, buoyancy (gravity) waves, rotationally modified (e.g., Kelvin & Rossby) waves, and horizontally propagating sound waves, but they filter vertically propagating sound waves. The horizontal momentum, vertical momentum, mass continuity, and thermodynamic energy equations are as follows (e.g., Kalnay 2003, pp. 60–67):

$$\frac{d\mathbf{v}}{dt} = -\nabla\Phi - f\mathbf{k} \times \mathbf{v}, \quad (1)$$

$$\frac{\partial\Phi}{\partial p} = -\frac{1}{\rho}, \quad (2)$$

$$\nabla \cdot \mathbf{v} + \frac{\partial\omega}{\partial p} = 0, \quad (3)$$

$$\frac{dT}{dt} = \frac{q}{c_p} + \frac{\omega}{\rho c_p}, \quad (4)$$

where  $\mathbf{v}$  is the horizontal velocity on constant-pressure surfaces,  $\omega \equiv dp/dt$  is the vertical velocity in pressure coordinates,  $\Phi$  is the gravitational potential on constant-pressure surfaces,  $f \equiv 2\Omega \sin \phi$  is the Coriolis parameter,  $\Omega$  is the planetary rotation rate ( $2\pi$  over the rotation period),  $\mathbf{k}$  is the local vertical unit vector,  $q$  is the thermodynamic heating rate ( $\text{W kg}^{-1}$ ), and  $T$ ,  $\rho$ , and  $c_p$  are the temperature, density, and specific heat at constant pressure.  $\nabla$  is the horizontal gradient evaluated on constant-pressure surfaces, and  $d/dt = \partial/\partial t + \mathbf{v} \cdot \nabla + \omega\partial/\partial p$  is the material derivative. Curvature terms are included in  $\mathbf{v} \cdot \nabla\mathbf{v}$ . Equation (4) is actually solved in an alternate form,  $d\theta/dt = q\theta/(c_p T)$ , where  $\theta \equiv T(p_0/p)^\kappa$  is the “potential temperature” (a measure of entropy),  $\kappa$  is the ratio of the gas constant to specific heat at constant pressure, and  $p_0$  is a reference pressure, taken as 1 bar (note, however, that the dynamics are independent of the choice of  $p_0$ ). The dependent variables  $\mathbf{v}$ ,  $\omega$ ,  $\Phi$ ,  $\rho$ ,  $T$ , and  $\theta$  are functions of longitude  $\lambda$ , latitude  $\phi$ , pressure  $p$ , and time  $t$ .

Note that the vertical velocity is nonzero—it enters via the mass-continuity equation and the thermodynamic energy equation. For a known atmospheric state at a given time step, equations (1) and (4) are integrated forward, leading to expressions for  $\mathbf{v}$  over the 3D grid at the subsequent time step. The horizontal divergence of these velocities is generally nonzero, and the vertical velocity  $\omega$  is then evaluated for that time step via equation (3) with use of the boundary conditions. For conditions relevant to hot Jupiters, the characteristic vertical velocity is typically  $\sim 10 \text{ m s}^{-1}$  near the photosphere (Showman & Guillot 2002; Cooper & Showman 2006; see also § 6).

The ARIES/GEOS dynamical core discretizes the equations in longitude and latitude using an Arakawa C grid (Arakawa & Lamb 1977) and adopts a pressure coordinate in the vertical. The top boundary condition is constant pressure and the bottom boundary condition is an impermeable surface, which we place far below the region of interest. These boundaries are free-slip in horizontal velocity. We solve the equations using horizontal resolutions in longitude and latitude of  $72 \times 45$  or  $144 \times 90$  with 30–40 layers spaced evenly in  $\log p$ . The ARIES/GEOS model has been widely used in Earth and Mars studies and has been successfully benchmarked against standard test cases (Held & Suarez 1994). Although

our specific implementation of the ARIES/GEOS code has yet to be applied to planets in our solar system beyond the Earth Held-Suarez test case, we emphasize that the 3D primitive equations have been successfully used to model the global circulation of Earth, Mars, Venus, Titan, and the giant planets in our solar system, forced both by simplified Newtonian heating/cooling (Held & Suarez 1994; Haberle et al. 1997; Houben et al. 1997; Lee et al. 2007; Hernstein & Dowling 2007; Yamamoto & Takahashi 2003, 2006; Williams 2003; Lian & Showman 2008<sup>9</sup>) and, in the case of Earth, Mars, and Titan, by realistic radiative transfer (e.g., Haberle et al. 1993; Basu et al. 2006; Newnam et al. 2002; Forget et al. 1999; Tokano et al. 2001; Hourdin et al. 1995).

Our simulations contain no explicit viscosity, but to maintain numerical stability, we apply at each time step a fourth-order Shapiro filter (Shapiro 1970) to the time derivative of potential temperature and an eighth-order Shapiro filter to the time derivative of the horizontal velocity components. This filter, which is analogous to a hyperviscosity, horizontally smooths grid-scale variations while leaving long-wavelength structures relatively unaffected. To maintain stability near the poles, we apply additional grid-scale smoothing in longitude using a polar filter (Suarez & Takacs 1995). This is applied to the time derivatives of potential temperature and horizontal velocity poleward of  $45^\circ$  latitude. In all cases, the smoothing is applied to the time derivatives immediately before these derivatives are used to update the variables at the next time step. Both filters are standard practice in atmospheric circulation studies.

For HD 209458b, we adopt gravity, planetary radius, and rotation rate  $\Omega$  of  $9.81 \text{ m s}^{-2}$ ,  $9.44 \times 10^7 \text{ m}$ , and  $2.06 \times 10^{-5} \text{ s}^{-1}$ , respectively (implying a rotation period of 3.5 days). The corresponding values for HD 189733b are  $22.62 \text{ m s}^{-1}$ ,  $8.22 \times 10^7 \text{ m}$ , and  $3.29 \times 10^{-5} \text{ s}^{-1}$ , respectively (implying a rotation period of 2.2 days). For both planets,  $c_p = 1.23 \times 10^4 \text{ J kg}^{-1} \text{ K}^{-1}$  and the molar mass is  $2.36 \times 10^{-3} \text{ kg mol}^{-1}$ , implying a specific gas constant,  $R$ , of  $3523 \text{ J kg}^{-1} \text{ K}^{-1}$ . We adopt the ideal gas equation of state.

The top layer is placed at 0.7 mbar. Radiative calculations that match the planetary radius suggest that the temperature profiles converge to the interior adiabat at  $\sim 50$  bars on HD 209458b and  $\sim 500$  bars on HD 189733b (Fig. 1). Accordingly, we place the bottom pressure at 100 bars for HD 209458b and 900 bars for HD 189733b. This means that the deepest  $\sim 3$  model layers are in the neutrally stable convective region (i.e., these layers have zero Brunt-Väisälä frequency). Including these layers in our model gives the overlying radiative zone room to deform vertically and limits artificial behavior that might occur if the base of the model were too close to the photosphere. Nevertheless, we note that the primitive equations do not account for the small-scale convective motions that occur in the convective region; these bottom layers are best viewed as representing a neutrally stable bottom boundary condition for the overlying weather-layer dynamics. The initial conditions contain no winds and adopt a temperature profile resulting from a 1D global-average radiative-transfer calculation of the planet. Our basic results are insensitive to the initial condition, as is discussed more fully in § 3.

The heating rate is

$$\frac{q}{c_p} = \frac{T_{\text{eq}}(\lambda, \phi, p) - T(\lambda, \phi, p, t)}{\tau_{\text{rad}}(p, T)}. \quad (5)$$

We assume that the obliquity and orbital eccentricity are zero, and that the planet rotates synchronously, which implies that the

<sup>9</sup> See also Y. Lian & A. P. Showman at <http://www.asiaoceania.org/aogs2008>.

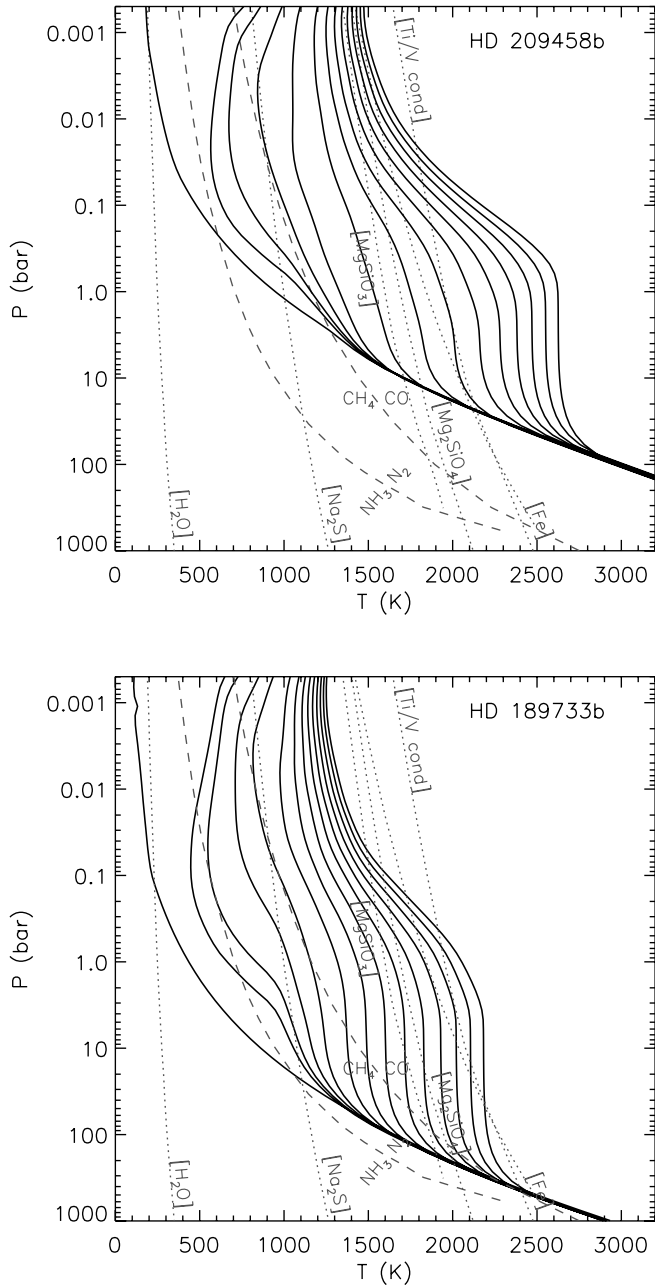


FIG. 1.—Pressure-temperature ( $p$ - $T$ ) profiles for planet HD 209458b (*top*) and HD 189733b (*bottom*) as a function of  $\mu$ . The hottest profile is  $\mu = 1.0$ , and the profiles decrease in steps of 0.1 to  $\mu = 0.1$ . Profiles for  $\mu = 0.05, 0.02, 0.01$  are also shown, as well as the nonirradiated nightside profile ( $\mu = 0$ ). The profiles are radiative at the top and convective at the bottom (where they all converge to the same convective adiabat). Condensation curves are shown as dotted lines and are labeled. Equal abundance curves for CO/CH<sub>4</sub> and N<sub>2</sub>/NH<sub>3</sub> are dashed.

radiative-equilibrium temperatures  $T_{\text{eq}}(\lambda, \phi, p)$  and radiative time constants  $\tau_{\text{rad}}(p, T)$  are time-independent; the following subsection describes how we calculate them. The substellar latitude and longitude remain fixed at  $0^\circ, 0^\circ$  throughout the simulation.

## 2.2. Radiative-Equilibrium Temperature Structures

We specify  $T_{\text{eq}}$  in equation (5) by calculating the radiative-equilibrium temperatures as a function of longitude, latitude, and pressure for conditions relevant to HD 209458b and HD 189733b. To do so, we calculate atmospheric pressure-temperature ( $p$ - $T$ ) profiles using a variant of the plane-parallel multistream radiative transfer code first used for Titan by McKay et al. (1989) and

later extended to giant planets and brown dwarfs by Marley, Fortney, and collaborators (Marley et al. 1996, 1999; Burrows et al. 1997; Marley & McKay 1999; Fortney et al. 2005, 2006a, 2006b). Although the metallicities of HD 209458b and HD 189733b are unknown, the host stars have near-solar metallicity. Here we adopt solar metallicity for the planets and assume local chemical equilibrium (Lodders & Fegley 2002, 2006). The calculations use a large and continually updated opacity database described in Freedman et al. (2008). For these exploratory calculations we neglect cloud opacity, although the “rainout” of elements that condense into clouds is always properly accounted for.

For the present calculations, the opacities of TiO and VO are excluded, as has been standard for models of multi-Gyr-old hot Jupiters at the incident flux levels expected for gas giants beyond  $\sim 0.03$  AU (for a Sun-like primary). One-dimensional atmosphere models suggest that gaseous TiO and VO are cold trapped at pressures of  $\sim 10$ – $100$  bars where solid clouds incorporating Ti and V form, which suggests that TiO and VO should be absent in the observable atmosphere (e.g., Hubeny et al. 2003; Fortney et al. 2006b). However, the recent detection of a hot dayside stratosphere on HD 209458b (Knutson et al. 2008) suggests that future studies of this planet should include TiO and VO (Burrows et al. 2007b; Fortney et al. 2007). The limited data for HD 189733b are consistent with no TiO/VO opacity (Fortney & Marley 2007).

The code treats thermal radiation from the planet from  $0.26$ – $325 \mu\text{m}$  and incident radiation from the parent star from  $0.26$ – $6.0 \mu\text{m}$ . The calculation of  $T_{\text{eq}}$  is performed at 60 model layers from  $0.3$  mbar to 1000 bars, although the opacities at  $p > 100$  bars are quite uncertain owing to imperfect knowledge of the line broadening under these conditions. The calculation includes incident flux from the parent star, thermal flux from the planet’s atmosphere, and thermal flux from the planet’s interior, parameterized by  $T_{\text{int}}$ , the intrinsic effective temperature.

To calculate radiative-equilibrium  $p$ - $T$  profiles, we take an approach similar to that of Barman et al. (2005). At a given location on the planet’s dayside, the incident stellar flux arrives with an angle  $\theta$  from the local vertical. The cosine of this angle,  $\mu$ , varies from 1 at the substellar point to 0 at the terminator. Large  $\mu$  allows deeper penetration of stellar flux, greater absorption, and a warmer atmosphere. Smaller  $\mu$  gives a longer path length and air mass to a given pressure, implying shallower penetration of flux, less absorption (greater scattering), and a cooler atmosphere. We calculate  $p$ - $T$  profiles for concentric rings of atmosphere that are symmetric around the normal at the subsolar point. The profiles are calculated at  $\mu = 1.0, 0.9, 0.8, 0.7, 0.6, 0.5, 0.4, 0.3, 0.2, 0.1, 0.05, 0.02, 0.01$ , and 0.0. The latter case, which is the radiative-equilibrium profile for an isolated object with the planet’s known radius, gives the radiative-equilibrium profile across the entire nightside. All cases use a constant specific entropy at the bottom boundary, corresponding to the value needed to reproduce the planetary radius with an assumed heavy-element abundance of  $\sim 30$ – $40$  Earth masses in the planetary interior, similar to that of Jupiter (Saumon & Guillot 2004).

The top and bottom panels of Figure 1 depict the resulting profiles for HD 209458b and HD 189733b, respectively. These atmospheric  $p$ - $T$  profiles show the atmosphere structure that each planet would attain under radiative equilibrium. The large temperature gradients implied on the planetary dayside shows that vigorous dynamics is expected to occur. In chemical equilibrium, CO would dominate over CH<sub>4</sub> across much of the dayside, but CH<sub>4</sub> would dominate on the nightside. In the absence of any energy redistribution, the nightsides of these planets would be quite cold, with 100 mbar temperatures of 500 and 200 K for HD 209458b and HD 189733b, respectively. The nightside

heavy-element composition would be dominated by  $\text{H}_2\text{O}$ ,  $\text{CH}_4$ , and  $\text{NH}_3$ , and would be devoid of atomic alkalis, which would condense into clouds. Perhaps  $\text{H}_2\text{O}$  cloud condensation would occur as well. Dynamical redistribution of energy will of course alter the atmospheric temperature structure and chemistry.

### 2.3. Radiative Timescales

We developed a simple method for calculating the temperature and pressure-dependent radiative timescales across the large  $p$ - $T$  space accessed by these atmospheres. We first calculate a suite of converged radiative-convective model atmospheres similar to those shown in Figure 1. In calculating these profiles, we assumed  $\mu = 0.5$ , corresponding to dayside-average conditions, but we adjust the stellar flux to give a range of incident top-of-atmosphere stellar fluxes (different for each profile) corresponding to that spanned by the profiles in Figure 1. Like those in Figure 1, the resulting  $p$ - $T$  profiles span temperatures ranging from  $\sim 100$  to 2500 K for both planets.

Although our radiative-transfer code is not a time-dependent solver, we can still calculate the radiative time constants as follows. For each one of the  $p$ - $T$  profiles, we add a thermal perturbation  $\delta T = 10$  K to a given model layer with pressure  $p_0$ . Because this perturbed profile deviates from radiative equilibrium, the perturbed layer emits a different flux than it receives, implying a cooling/heating that should cause the thermal perturbation to decay. Given the perturbed profile, we perform a radiative-transfer calculation (without iteration) to calculate the net flux versus height for that profile. For any function  $f(t)$ , a characteristic timescale for variation of  $f$  is  $f(df/dt)^{-1}$  (for exponential decay this would simply give the  $e$ -folding timescale). Thus, we simply calculate the characteristic timescale for decay of the thermal perturbation as  $\delta T$  divided by the heating rate expressed in  $\text{K s}^{-1}$ , namely,

$$\tau_{\text{rad}} = \delta T \frac{\rho c_p}{dF/dz}, \quad (6)$$

where  $F$  is the net vertical radiative flux,  $\rho$  is density,  $z$  is height, and  $dF/dz$  is the volumetric heating rate ( $\text{W m}^{-3}$ ). By varying  $p_0$ , we can calculate  $\tau_{\text{rad}}$  as a function of pressure for every  $p$ - $T$  profile in our suite of models.

Figure 2 shows the resulting  $\tau_{\text{rad}}$  for HD 209458b and HD 189733b. These are surfaces on a regular  $p$ - $T$  grid, interpolated from the original calculations. Some modest extrapolation was done on the high  $T$ /low  $p$  and low  $T$ /high  $p$  corners. Perhaps the most striking aspect of the calculations is the strong pressure dependence, with  $\tau_{\text{rad}}$  values changing by 8 orders of magnitude at a given temperature, from millibars to hundreds of bars in pressure. Temperature effects are also substantial. At millibar pressures we find a 6 orders of magnitude change in  $\tau_{\text{rad}}$  across the temperatures that we explore, with the most significant temperature dependence coming below  $\sim 500$  K, where  $\tau_{\text{rad}}$  becomes quite long. The calculations for HD 189733b extend to higher pressures than HD 209458b because of the expected deeper radiative zone in the atmosphere of HD 189733b. On average, the values for HD 209458b slightly exceed those for HD 189733b (by a factor of 1.5–3). This results from the lower gravity for HD 209458b, which leads to a “puffed up” atmosphere with greater mass per area across a given pressure interval.

We ran tests to determine the sensitivity of our  $\tau_{\text{rad}}$  calculation to the magnitude and thickness of the adopted temperature perturbation. Tests with  $\delta T = 5, 10, 20, 50,$  and  $100$  K yielded nearly identical results for  $\tau_{\text{rad}}$ , consistent with expectations for the low-amplitude (linear) limit. However, for  $\delta T = 200$  and  $400$  K, the calculated  $\tau_{\text{rad}}$  values were factors of  $\sim 1.3$  and  $2$  shorter,

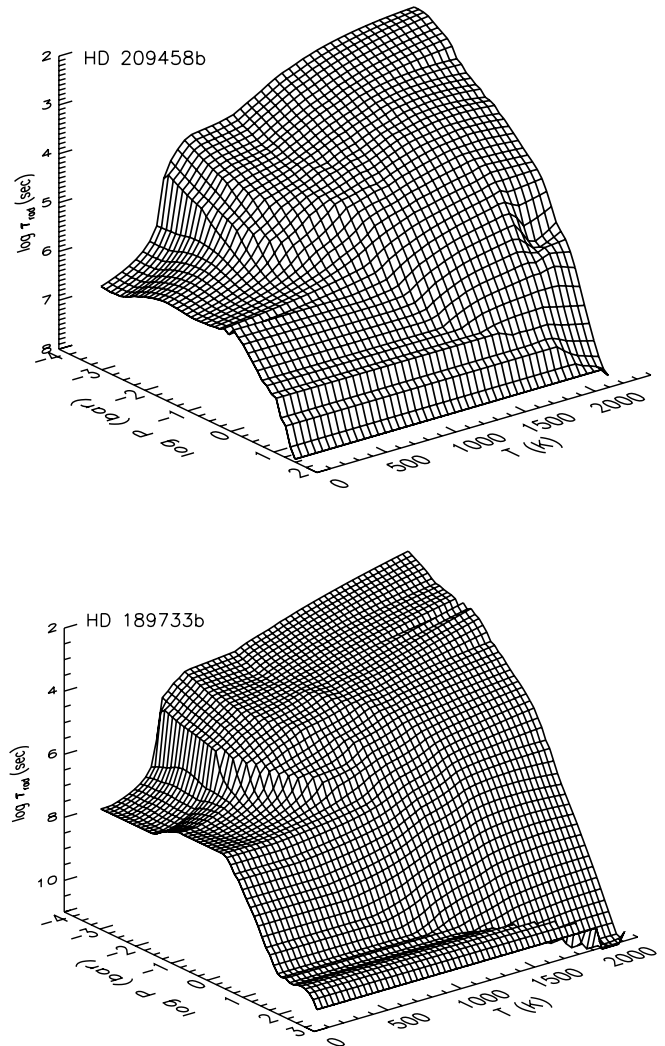


FIG. 2.—Radiative time constant ( $\tau_{\text{rad}}$ ) as function of pressure and temperature in the atmosphere of HD 209458b (top) and HD 189733b (bottom). Time constants were derived from  $p$ - $T$  profiles computed as described in the text. Small-scale, low-amplitude bumpy structure in the surfaces results from the interpolation of the  $\tau_{\text{rad}}$  values onto a regular  $p$ - $T$  grid; this small-scale bumpiness is not physically relevant and does not have a significant influence on our results.

respectively, than that calculated for the smaller  $\delta T$  values. We also ran tests that held  $\delta T$  constant but varied the vertical thickness of the perturbation from 0.3 to 1 scale height. Across this range,  $\tau_{\text{rad}}$  varied by a factor of  $\sim 2$ – $3$  at the pressures relevant for *Spitzer* emission spectra (1–100 mbar), increasing to nearly an order of magnitude at  $p > 1$  bar. Because deviations from radiative equilibrium in the real atmosphere will not follow the idealized shapes adopted here, our  $\tau_{\text{rad}}$  values should therefore be viewed as uncertain to an order of magnitude.

To our knowledge the only previous calculation of radiative time constants over a wide range in atmospheric pressure for hot Jupiters was by Iro et al. (2005) for HD 209458b. These calculations were limited to  $\tau_{\text{rad}}$  as a function of  $p$  only along the 1D atmospheric  $p$ - $T$  profile that these authors calculated for the planet. Iro et al. (2005) determined  $\tau_{\text{rad}}$  by adding Gaussian temperature perturbations to their previously converged radiative equilibrium profile. They then performed a time-dependent radiative-transfer calculation to explicitly simulate the characteristic time needed for their model atmosphere to relax back to the radiative equilibrium structure. Our  $p$ - $T$ - $\tau_{\text{rad}}$  surfaces shown in Figure 2 cover a much larger phase space than was explored by these authors.

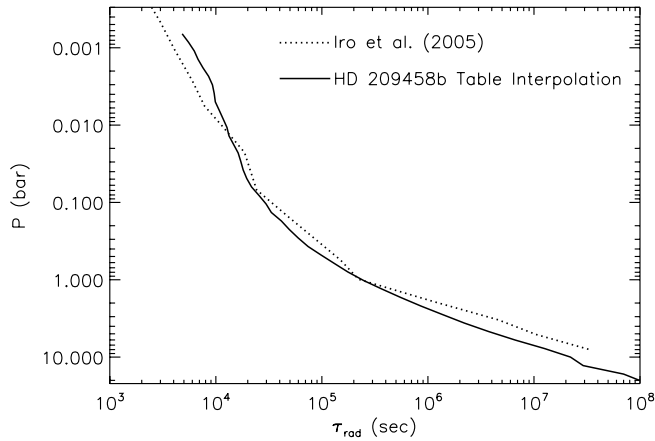


FIG. 3.— Comparison of the radiative time constant ( $\tau_{\text{rad}}$ ) as function of pressure for the atmospheric  $p$ - $T$  profile of HD 209458b from Iro et al. (2005). The dotted curve is the  $\tau_{\text{rad}}$  calculation from Iro et al. (2005). The solid curve is an interpolation of our  $\tau_{\text{rad}}$  results from our  $p$ - $T$ - $\tau_{\text{rad}}$  grid for HD 209458b (shown in Fig. 2) onto the Iro et al.  $p$ - $T$  profile.

Although our chosen methods are quite different, Figure 3 shows that our derived  $\tau_{\text{rad}}$  values for the 1D profile from Iro et al. (2005) are actually very similar. Tabulated values of  $\tau_{\text{rad}}$  as a function of  $p$  and  $T$  for planets HD 209458b and HD 189733b are found in Tables 1 and 2.

### 3. RESULTS: DYNAMICAL SIMULATIONS

#### 3.1. Flow Regime and Dependence on Parameters

Consistent with the results of Cooper & Showman (2005); Cooper & Showman (2006) the imposed day-night heating contrasts lead to rapid development of large day-night temperature differences and winds reaching several  $\text{km s}^{-1}$ . Figures 4–5 show the temperature (*gray scale*) and horizontal winds (*arrows*) for

our nominal simulations of HD 189733b and HD 209458b at times of 900 and 800 days, respectively, by which time the temperature and wind patterns have reached a quasi-steady state at  $p < 1$  bar. Panels are shown at pressures of 10 mbar, 100 mbar, and 1 bar, which bracket the range of pressures expected to be important for observable spectra and light curves. Both simulations use a resolution of  $144 \times 90$  with 30 layers.

As expected, the flow develops patterns of temperature and wind that vary horizontally and vertically in an inherently 3D manner. At low pressure ( $p \leq 10$  mbar), the radiative time constants are shorter than the typical time for wind to advect across a hemisphere, and so the temperature patterns track the stellar heating—hot on the dayside and cold on the nightside, with approximate boundaries at the terminators (longitudes  $\pm 90^\circ$ ). The predominant flow pattern moves air away from the substellar point toward the antistellar point, both along the equator and over the poles. At deeper levels, the flow forms a banded structure dominated by an eastward equatorial jet extending from latitude  $\sim 30^\circ\text{N}$  to  $30^\circ\text{S}$  (Figs. Fig. 4 and 5, *middle and bottom panels*). In the range  $\sim 50$ –300 mbar, the advection times are similar to the radiative times, leading to large longitudinal temperature differences whose patterns are distorted from the day-night heating patterns; at  $p \geq 1$  bar, however, the radiative timescale is longer than the longitudinal advection time and temperatures become homogenized in longitude. The advection times in latitude exceed those in longitude, so nonzero latitudinal temperature differences persist even at relatively deep levels (Figs. 4 and 5, *bottom panels*). This banded structure results directly from the effects of planetary rotation, as has been shown by previous authors (Showman et al. 2007; Showman & Guillot 2002; Cho et al. 2003, 2008; Menou et al. 2003; Cooper & Showman 2005; Dobbs-Dixon & Lin 2008).

Consistent with the results of previous studies (Showman & Guillot 2002; Menou et al. 2003; Cho et al. 2003, 2008; Langton & Laughlin 2007; Dobbs-Dixon & Lin 2008), the horizontal length scales of the simulated circulation patterns are comparable to a

TABLE 1  
RADIATIVE TIME CONSTANTS FOR HD 209458b

$P$ (bar)	400	600	800	1000	1200	1400	1600	1800	2000	2200
0.00066.....	6.05e+05	1.16e+04	6.36e+03	4.85e+03	2.33e+03	1.19e+03	7.38e+02	5.40e+02	4.38e+02	3.83e+02
0.00110.....	6.16e+05	1.51e+04	8.24e+03	6.50e+03	2.99e+03	1.56e+03	9.47e+02	6.60e+02	5.04e+02	4.11e+02
0.00182.....	5.99e+05	1.99e+04	1.03e+04	8.10e+03	3.90e+03	2.03e+03	1.24e+03	8.52e+02	6.47e+02	5.25e+02
0.00302.....	5.20e+05	2.69e+04	1.30e+04	1.05e+04	5.12e+03	2.76e+03	1.68e+03	1.15e+03	8.72e+02	7.11e+02
0.00501.....	4.49e+05	3.51e+04	1.56e+04	1.21e+04	6.36e+03	3.49e+03	2.14e+03	1.52e+03	1.21e+03	1.04e+03
0.00832.....	4.20e+05	4.75e+04	1.97e+04	1.50e+04	8.58e+03	4.80e+03	2.89e+03	2.12e+03	1.85e+03	1.82e+03
0.01380.....	4.21e+05	6.34e+04	2.59e+04	1.78e+04	1.07e+04	6.39e+03	3.96e+03	2.85e+03	2.59e+03	2.72e+03
0.02291.....	4.57e+05	8.48e+04	3.37e+04	2.29e+04	1.52e+04	9.13e+03	5.57e+03	3.93e+03	3.49e+03	3.66e+03
0.03802.....	5.49e+05	1.16e+05	4.72e+04	2.84e+04	1.82e+04	1.26e+04	7.14e+03	5.39e+03	4.79e+03	5.06e+03
0.06310.....	6.72e+05	2.45e+05	8.12e+04	3.52e+04	2.49e+04	1.77e+04	1.03e+04	7.87e+03	6.97e+03	7.42e+03
0.10471.....	7.98e+05	4.16e+05	1.45e+05	5.89e+04	3.45e+04	2.61e+04	1.61e+04	1.17e+04	1.01e+04	1.09e+04
0.17378.....	8.85e+05	5.81e+05	2.76e+05	1.33e+05	5.60e+04	4.03e+04	2.69e+04	1.92e+04	1.69e+04	1.77e+04
0.28840.....	9.35e+05	7.01e+05	4.67e+05	2.51e+05	1.04e+05	6.93e+04	4.76e+04	3.52e+04	2.67e+04	2.89e+04
0.47863.....	9.14e+05	7.71e+05	6.28e+05	4.84e+05	2.40e+05	1.30e+05	9.06e+04	6.68e+04	4.92e+04	4.82e+04
0.79433.....	...	...	1.02e+06	9.15e+05	6.17e+05	2.91e+05	1.82e+05	1.32e+05	1.03e+05	1.28e+05
1.31826.....	...	...	...	1.63e+06	1.50e+06	6.82e+05	4.03e+05	3.00e+05	2.43e+05	5.90e+05
2.18776.....	...	...	...	3.02e+06	2.99e+06	1.76e+06	1.00e+06	7.67e+05	6.93e+05	7.37e+05
3.63078.....	...	...	...	...	5.79e+06	4.59e+06	2.61e+06	2.06e+06	1.70e+06	1.66e+06
6.02560.....	...	...	...	...	...	8.87e+06	8.06e+06	6.51e+06	6.19e+06	8.65e+06
10.00000.....	...	...	...	...	...	...	...	2.21e+07	2.17e+07	3.60e+07
16.59590.....	...	...	...	...	...	...	...	...	7.01e+07	9.39e+07

NOTE.— Column headings are temperatures in kelvin. Values are time constants in seconds. Note that no values were calculated in the lower left corner here and in Table 2 because the radiative-equilibrium  $p$ - $T$  profiles used to calculate  $\tau_{\text{rad}}$  (Fig. 1) do not access these pressure/temperature combinations.

TABLE 2  
RADIATIVE TIME CONSTANTS FOR HD 189733b

$P$ (bar)	400	600	800	1000	1200	1400	1600	1800	2000
0.00066.....	2.58e+06	7.40e+03	4.84e+03	3.33e+03	1.61e+03	7.84e+02	4.25e+02	2.45e+02	1.49e+02
0.00110.....	1.87e+06	9.32e+03	6.48e+03	4.25e+03	2.08e+03	1.03e+03	5.73e+02	3.38e+02	2.09e+02
0.00182.....	1.53e+06	1.19e+04	8.42e+03	5.44e+03	2.65e+03	1.34e+03	7.58e+02	4.58e+02	2.91e+02
0.00302.....	1.11e+06	1.54e+04	1.07e+04	7.13e+03	3.43e+03	1.78e+03	1.05e+03	6.66e+02	4.48e+02
0.00501.....	9.54e+05	1.94e+04	1.22e+04	8.34e+03	4.26e+03	2.28e+03	1.35e+03	8.60e+02	5.76e+02
0.00832.....	1.05e+06	2.54e+04	1.42e+04	1.01e+04	5.50e+03	3.00e+03	1.77e+03	1.11e+03	7.24e+02
0.01380.....	1.34e+06	3.27e+04	1.69e+04	1.14e+04	6.79e+03	3.82e+03	2.25e+03	1.39e+03	8.95e+02
0.02291.....	1.78e+06	4.30e+04	2.05e+04	1.27e+04	8.95e+03	5.31e+03	2.93e+03	1.67e+03	9.79e+02
0.03802.....	1.86e+06	5.77e+04	2.56e+04	1.44e+04	1.12e+04	7.00e+03	3.94e+03	2.18e+03	1.20e+03
0.06310.....	2.22e+06	8.71e+04	3.64e+04	2.08e+04	1.39e+04	8.90e+03	5.38e+03	3.12e+03	1.80e+03
0.10471.....	2.55e+06	1.44e+05	5.11e+04	3.02e+04	1.76e+04	1.33e+04	7.97e+03	5.15e+03	3.39e+03
0.17378.....	3.55e+06	2.43e+05	1.03e+05	5.55e+04	2.74e+04	1.88e+04	1.23e+04	8.52e+03	6.20e+03
0.28840.....	4.55e+06	7.25e+05	2.40e+05	1.00e+05	5.43e+04	3.01e+04	1.97e+04	1.42e+04	1.07e+04
0.47863.....	5.60e+06	2.17e+06	4.30e+05	2.33e+05	9.63e+04	4.94e+04	3.52e+04	2.58e+04	2.02e+04
0.79433.....	6.64e+06	3.78e+06	9.20e+05	5.28e+05	2.15e+05	1.03e+05	6.57e+04	4.76e+04	3.63e+04
1.31826.....	7.61e+06	5.50e+06	3.39e+06	1.47e+06	5.06e+05	2.58e+05	1.30e+05	9.42e+04	7.01e+04
2.18776.....	9.59e+06	7.73e+06	5.87e+06	4.02e+06	1.34e+06	6.56e+05	2.89e+05	2.07e+05	1.52e+05
3.63078.....	2.52e+07	2.03e+07	1.47e+07	9.04e+06	3.74e+06	1.68e+06	6.95e+05	5.34e+05	4.36e+05
6.02560.....	5.96e+07	5.22e+07	3.82e+07	2.42e+07	9.70e+06	4.37e+06	1.87e+06	1.52e+06	1.40e+06
10.00000.....	1.67e+08	1.61e+08	1.15e+08	6.87e+07	2.72e+07	1.30e+07	5.86e+06	5.08e+06	5.59e+06
16.59590.....	...	4.91e+08	3.83e+08	2.20e+08	8.97e+07	4.55e+07	2.18e+07	1.86e+07	1.97e+07
27.54230.....	...	1.80e+09	1.70e+09	8.98e+08	3.25e+08	1.70e+08	8.51e+07	6.80e+07	6.68e+07
45.70880.....	...	...	4.97e+09	3.54e+09	1.23e+09	6.43e+08	3.31e+08	2.60e+08	2.39e+08
75.85780.....	...	...	...	9.04e+09	4.69e+09	2.43e+09	1.30e+09	1.02e+09	8.98e+08
125.89300.....	...	...	...	1.02e+10	1.03e+10	8.99e+09	5.10e+09	3.98e+09	3.41e+09
208.92999.....	...	...	...	...	9.10e+09	1.05e+10	1.98e+10	1.51e+10	1.32e+10
346.73700.....	...	...	...	...	...	...	9.19e+09	5.67e+10	5.14e+10
575.44000.....	...	...	...	...	...	...	...	1.54e+10	1.30e+11

NOTE.—Column headings are temperatures in kelvin. Values are time constants in seconds.

planetary radius. This results from the fact that the Rhines length and the Rossby deformation radius, which tend to control the horizontal dimensions of the dominant flow structures, are comparable to a planetary radius for the modest rotation rates, high temperatures, and large static stabilities relevant here (Showman & Guillot 2002; Menou et al. 2003; Showman et al. 2007).

At  $p \leq 1$  bar, where radiative time constants are short (Fig. 2), the patterns of wind and temperature in our nominal simulations reach a quasi-steady state over short timescales of only  $\sim 25$  days. The flow continues to spin up over much longer timescales at depth, with the total kinetic energy integrated over the entire domain appearing to level off by  $\sim 1000$  days. Nevertheless, the radiative time constants at these great depths are extremely long, and it is possible that the deep kinetic energy could very slowly increase over times longer than integrated here. Long-time integrations will be needed to assess this situation. Regardless, we do not expect this issue to alter our basic conclusions in the observable atmosphere at  $p \leq 1$  bar.

The *qualitative* patterns of wind and temperature are similar in our HD 189733b and HD 209458b simulations, suggesting that these planets may have comparable circulation regimes despite modest (factor of 1.5–2) differences in gravity, rotation rate, and stellar flux. However, examination of Figures 4 and 5 shows that the *absolute* temperatures differ substantially between these cases. Our HD 209458b simulation produce minimum and maximum temperatures of  $\sim 400$  and  $\sim 1700$ – $1800$  K, respectively, in the observationally relevant layer from 10–1000 mbar. In contrast, our HD 189733b simulation is cooler, with temperatures ranging from 300 K to only  $\sim 1400$  K in this same layer. Although HD 189733b lies closer to its parent star (0.0313 AU as compared

to 0.046 AU for HD 209458b), the stellar luminosity is lower, explaining the cooler planetary temperatures.

A careful comparison of Figure 1 with Figures 4 and 5 shows how the actual temperatures compare to the radiative equilibrium temperatures. For HD 189733b, at low pressure ( $\sim 10$  mbar), the local radiative-equilibrium temperature  $T_{\text{eq}}$  ranges from 155 to 1340 K while the actual temperature ranges from  $\sim 300$  to 1300 K (fluctuating slightly in time). For HD 209458b, at this same pressure,  $T_{\text{eq}}$  ranges from 290 to 1670 K while the actual temperature ranges from 423 to 1687 K. Both these comparisons show that  $T$  lies very close to  $T_{\text{eq}}$  on the dayside, but that  $T$  is substantially warmer than  $T_{\text{eq}}$  on the nightside. This effect results directly from the temperature dependence of  $\tau_{\text{rad}}$ . At deeper levels, where  $\tau_{\text{rad}}$  is greater,  $T$  is substantially warmer than  $T_{\text{eq}}$  on the nightside and cooler than  $T_{\text{eq}}$  on the dayside.

Figure 6 shows temperature profiles from our nominal HD 209458b case. To better represent the broad-scale conditions relevant for spectra and light curves (to be discussed in § 4), the profiles have been averaged across a circular region  $45^\circ$  in radius centered at the substellar point (*solid curve*), longitude  $90^\circ$  (*dashed curve*), antistellar point (*dashed-dotted curve*), and longitude  $-90^\circ$  (*dotted curve*), all at the equator. The profiles demonstrate that dynamics exercises a zeroth-order influence on the vertical temperature structure. On the nightside (*dashed-dotted curve*), the intense radiative cooling leads to a temperature that decreases strongly with height. As the equatorial jet transports this air eastward to the terminator at longitude  $-90^\circ$  (*dotted curve*), deep regions (0.1 to several bars) have continued to cool. Intense stellar heating initiates as this air reaches the dayside, but this has an immediate effect only at low pressures where radiative time constants

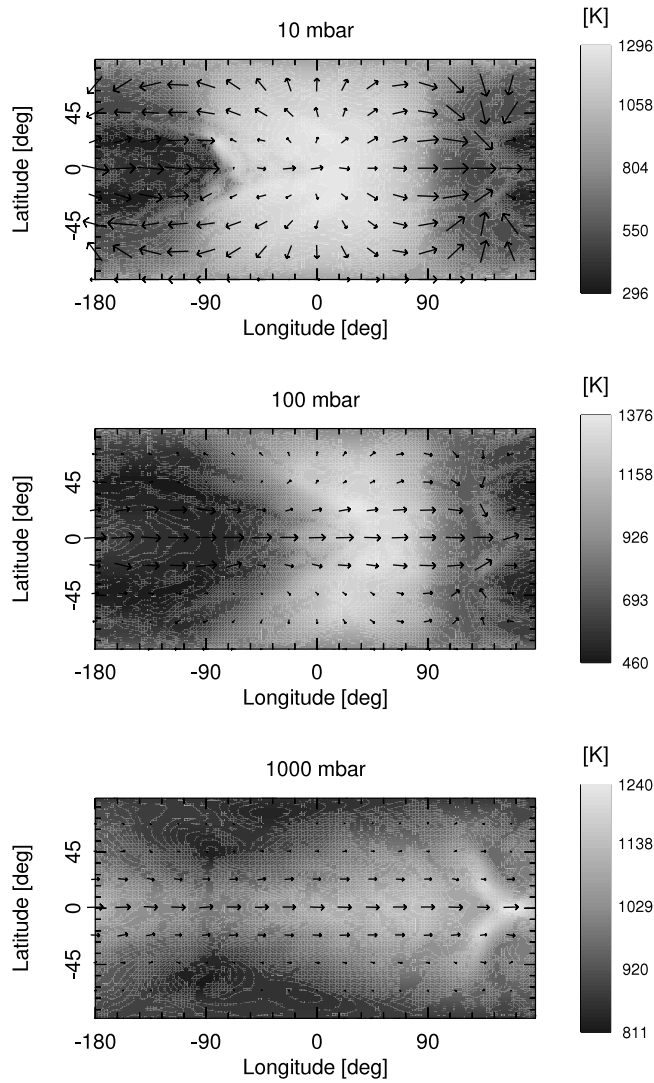


FIG. 4.— Temperature (*gray scale*) and winds (*arrows*) for nominal HD 189733b simulation at 900 days. Resolution is  $144 \times 90$ . For this and all simulations in this paper, the substellar point is at longitude, latitude ( $0^\circ, 0^\circ$ ); the terminators are at longitudes  $\pm 90^\circ$ .

are short. A thermal inversion thus develops at low pressures ( $< 50$  mbar). Westward flow at high latitudes and at pressures  $< 10$  mbar also contributes to this inversion, as such air comes from the hot dayside. By the time the superrotating equatorial jet transports the equatorial air eastward to the substellar region (*solid curve*), heating has had a substantial effect down to pressures of several hundred mbar, leading to a deep thermal inversion layer. As the air reaches the terminator at  $90^\circ$  longitude, rapid cooling aloft leads to low temperatures at pressures  $< 100$  mbar, but the layer between 0.1–1 bar has longer radiative time constants and, having just crossed the entire dayside hemisphere, remains warm. The key point is that the  $T(p)$  structure varies strongly across the globe and deviates strongly from the predictions of 1D radiative-equilibrium models, as previously described in Fortney et al. (2006a). The day-night temperature differences are  $\sim 300$  K at 1 bar,  $\sim 600$  K at 100 mbar, and increase to  $\sim 1000$  K at the top of the model.

To test the sensitivity of our results to model resolution, we also performed simulations of HD 209458b at a lower horizontal resolution of  $72 \times 45$  with 40 layers. These simulations produced patterns of wind and temperature that are nearly identical to Figure 5.

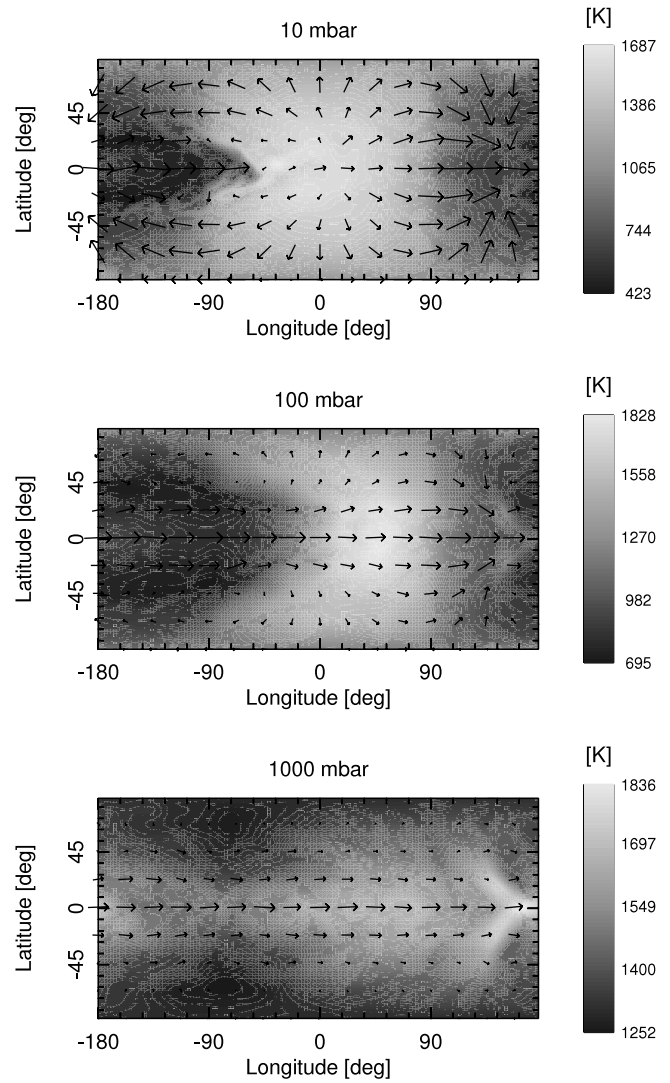


FIG. 5.— Temperature (*gray scale*) and winds (*arrows*) for HD 209458b simulation at 800 days. Resolution is  $144 \times 90$ .

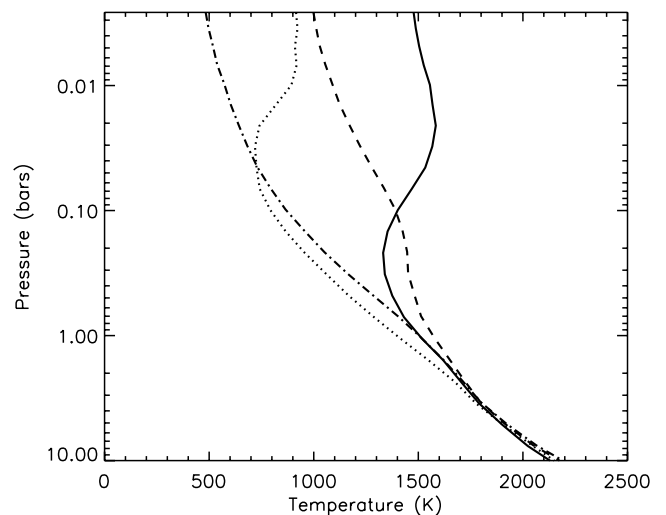


FIG. 6.— Temperature profiles for nominal HD 209458b case averaged across a disk  $45^\circ$  in radius centered at the substellar point (*solid curve*),  $90^\circ$  longitude (*dashed curve*), antistellar point (*dashed-dotted curve*), and  $-90^\circ$  longitude (*dotted curve*).

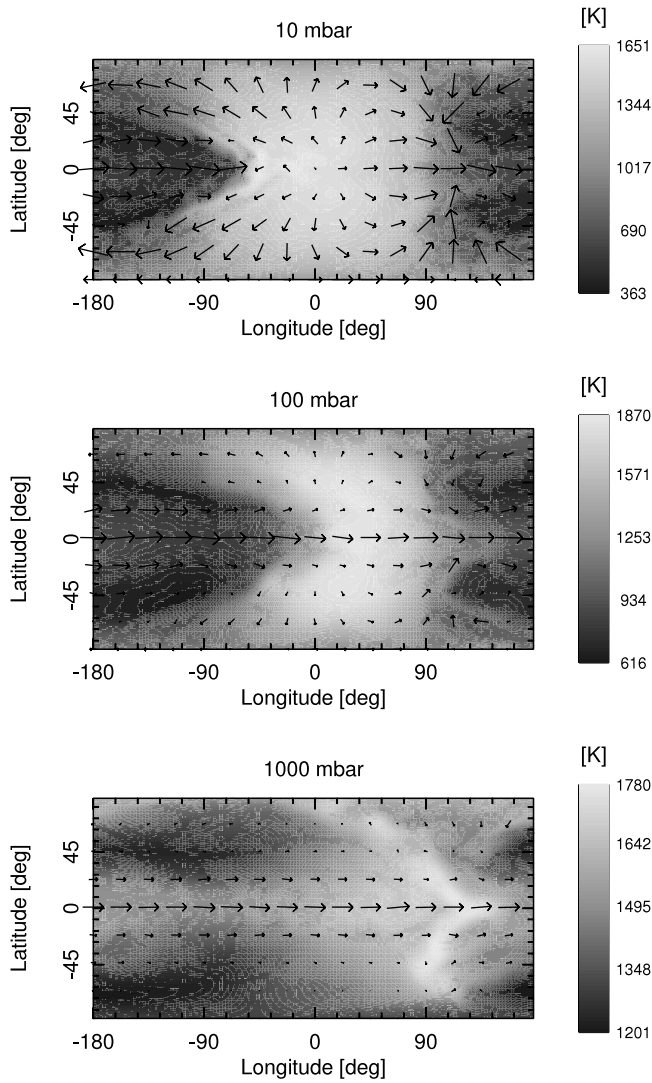


FIG. 7.— Temperature (gray scale) and winds (arrows) for HD 209458b simulation with twice the nominal  $\Omega$  at 800 days. Resolution is  $144 \times 90$ .

While we cannot rule out that the behavior could change at a resolution higher than considered here, this test suggests that, within the context of our forcing approach, our horizontal resolutions are sufficient to resolve the global-scale flow. This makes sense in light of the fact that (1) the predominant forcing consists of heating gradients with a large (hemispheric) length scale, and (2) the Rhines length and Rossby deformation radius, which determine the predominant horizontal widths of jets and baroclinic eddies, are comparable to the planetary radius. Our resolutions are sufficient to resolve these length scales. This differs from Jupiter, where a relatively fine horizontal resolution is required to resolve the small deformation radius of  $\sim 2000$  km.

To determine the influence of planetary rotation rate on the flow geometry, we performed HD 209458b parameter variations with double and half the nominal rotation rate (rotation periods of 1.75 and 7 days, respectively); the results are depicted in Figures 7 and 8. These models are otherwise essentially identical to the nominal HD 209458b case, including the use of an insolation pattern relevant for a synchronously rotating planet (i.e., the substellar point is locked at  $0^\circ$  longitude). Although the basic flow regimes are similar to those obtained in the nominal case (Fig. 5), a careful comparison reveals several key differences. Most importantly, as can best be seen at  $\sim 100$  mbar, the superrotating equatorial jet is narrower in the high rotation rate case (Fig. 7) and wider in the

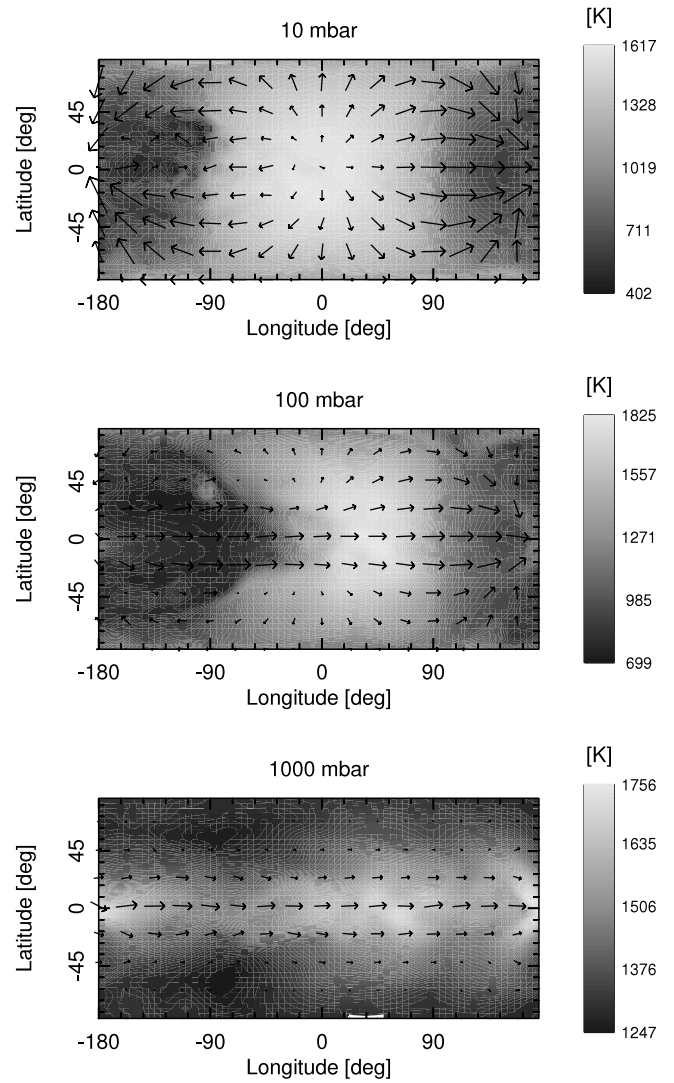


FIG. 8.— Temperature (gray scale) and winds (arrows) for HD 209458b simulation with half the nominal  $\Omega$  at 800 days. Resolution is  $72 \times 45$ .

low rotation rate case (Fig. 8) as compared to the nominal simulation. The midlatitude flow is, on balance, weaker at the higher rotation rates. Furthermore, the transition from simple dayside-to-nightside flow to a banded jet pattern occurs at lower pressures at the higher rotation rates. Figures 5 and 7 (top panels) develop equatorial flow that is eastward at most longitudes; on the other hand, Figure 8 (top) exhibits eastward flow at longitudes  $0^\circ$ – $180^\circ$  and westward flow at longitudes  $-100$  to  $0^\circ$ , leading to a pattern nearly symmetric in longitude about the substellar and antistellar points. As a result, substantial differences arise in the temperature and wind patterns at  $p \leq 100$  mbar in the nightside quadrant west of the antistellar point (longitudes  $90^\circ$ – $180^\circ$ ).

These differences in the jet patterns can be better appreciated by examining the plots of zonally averaged zonal wind shown in Figure 9. The top panel gives the nominal HD 209458b simulation (as in Fig. 5), and the middle and bottom panels depict the high and low rotation rate parameter variations (as in Figs. 7 and 8). The equatorial jets in the nominal and low rotation rate cases have latitudinal widths (characterized by FWHM) approximately 20% and 40% greater, respectively, than in the high rotation rate parameter variation. This agrees qualitatively with the expectation that, for constant wind speed, scale height, and static stability, faster rotation implies smaller Rhines length and Rossby deformation

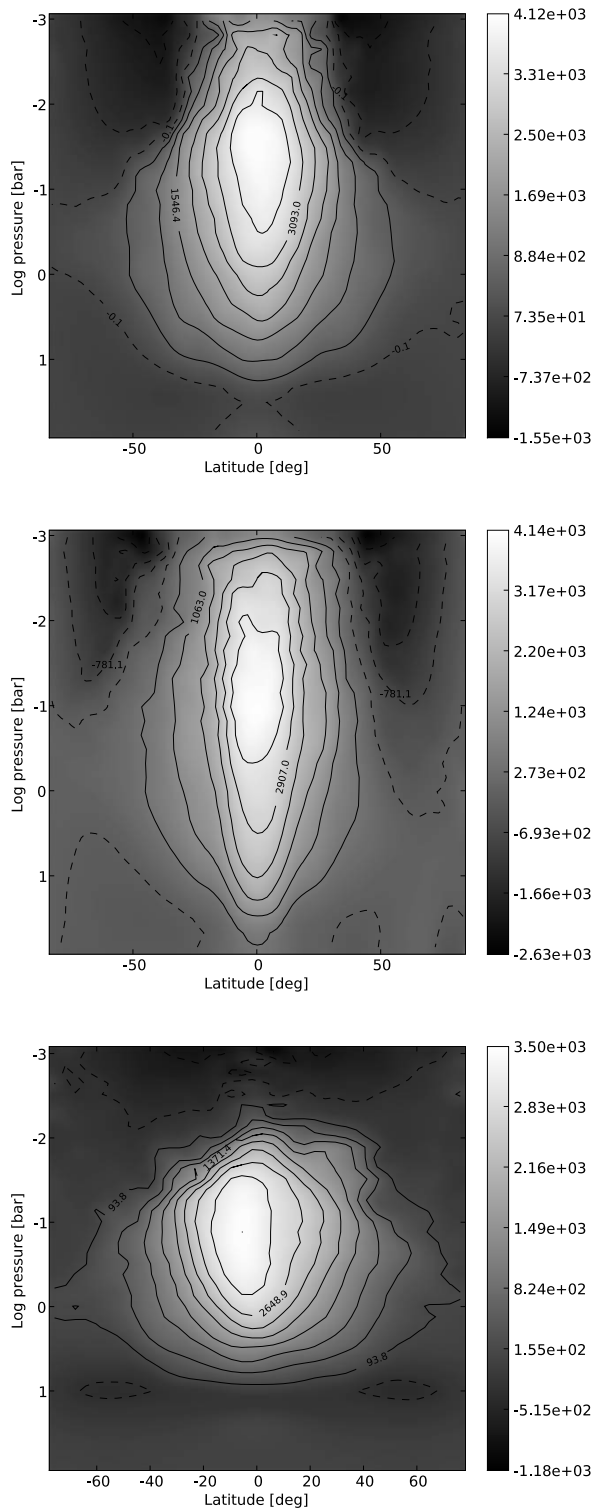


FIG. 9.—Zonal-mean zonal velocity vs. latitude and pressure for HD 209458b simulations at 800 days with nominal rotation rate (*top*), double the nominal rotation (*middle*) and half the nominal rotation (*bottom*). Scale bar shows wind speed in  $\text{m s}^{-1}$ ; positive is eastward and negative is westward. The equatorial jet is wider when the rotation rate is lower.

radius—and thus should lead to narrower jets. On the other hand, the simulated variations in jet width are less than suggested by Rhines scaling, which predicts that, at constant wind speed, factor of 4 variations in rotation rate should produce factor of 2 variations in jet width. The fact that the forcing length scale is similar

to the jet scale and that it remains constant throughout may play a role in muting the rotation-rate sensitivity. Interestingly, the jets penetrate slightly deeper in the higher rotation rate cases. The absence of the eastward jet at  $p < 10$  mbar in the low rotation rate case (Fig. 9, *bottom*) results from the fact that the flow is largely symmetric in longitude about the substellar point at these low pressures; the eastward and westward branches of the circulation cancel out in a zonal average, leading to weak zonal-mean wind speeds.

We also performed HD 209458b simulations with half and double the nominal gravity ( $5$  and  $20 \text{ m s}^{-2}$ ). These simulations are very similar to the nominal case shown in Figure 5, although the equatorial jet speed in the low-gravity case is slightly weaker than in the nominal and high-gravity cases.

To determine the sensitivity to the radiative time constant, we performed an HD 209458b simulation analogous to Figure 5 but multiplying  $\tau_{\text{rad}}$  by a factor of 10 at all temperatures and pressures. This case is particularly relevant because of the uncertainty in our calculated  $\tau_{\text{rad}}$ . This simulation, like our nominal case, develops a superrotating equatorial jet with weaker high-latitude flows. The simulation spins up to an approximate steady state at  $p < 1$  bar over about 100 days; kinetic energy at these levels remains essentially constant out to the end of our integration at 2000 days. In the quasi-steady state, the maximum zonal-mean zonal winds in the equatorial jet are  $2.8 \text{ km s}^{-1}$ , in comparison to  $4 \text{ km s}^{-1}$  for our case with nominal  $\tau_{\text{rad}}$  (Fig. 9). Likewise, the mass-weighted mean wind speed at  $p \leq 1$  bar (i.e.,  $(2K/M)^{1/2}$  where  $K$  and  $M$  are kinetic energy and mass integrated over  $p \leq 1$  bar) is  $420 \text{ m s}^{-1}$  for this case, as compared to  $770 \text{ m s}^{-1}$  for our case with nominal  $\tau_{\text{rad}}$ . At 100 mbar, the difference between maximum and minimum temperatures is  $\sim 400 \text{ K}$ , as compared to  $1100 \text{ K}$  for our nominal case; at this same pressure, the equivalent of Fig. 6 (where temperatures are averaged over a  $45^\circ$  radius) gives day-night temperature differences of  $240 \text{ K}$ , as compared to  $600 \text{ K}$  for our nominal case. Thus, increasing  $\tau_{\text{rad}}$  by a factor of 10 leads to weaker winds and more muted temperature differences. The temperature differences are smaller, despite weaker winds, simply because the net heating rate is lower. This is qualitatively consistent with simple scaling arguments (Showman & Guillot 2002), which predict day-night temperature differences and mean wind speeds that both scale as  $q^{1/2}$ , where  $q$  is a characteristic magnitude of the heating rate. Despite the differences in the details, we emphasize that the qualitative circulation pattern in this simulation strongly resembles that in our nominal cases.

We wish here to correct the record regarding the issue of sensitivity to initial conditions. Langton & Laughlin (2008) speculated that the simulated wind speeds reported in Cooper & Showman (2005) occurred because their simulations were initialized with the nightside temperature rather than the global-average temperature. This is incorrect. Our simulation results are insensitive to the initial temperature profile, particularly at pressures  $< 10$  bars; cold and hot initial temperatures lead to very similar end states. Simulations by Cooper & Showman (2006) explicitly demonstrate this fact: they initialized their simulations with the global-average temperature profile rather than the nightside temperature, yet their simulation results are nearly identical to those in Cooper & Showman (2005). This insensitivity occurs because the day-night temperature pattern that develops in the simulation (which via eqs. [1] and [2] determines the pressure-gradient forces that drive the winds) is dominated by the radiative heating/cooling patterns and hence quickly loses memory of its initial condition.

Likewise, Cooper & Showman (2005) showed that the same basic flow pattern emerges regardless of whether the atmosphere is initialized at rest or with a fast *westward* jet: both cases develop

strong superrotation with speeds of a few  $\text{km s}^{-1}$ . This suggests that the flow pattern is not strongly sensitive to the initial wind field. Nevertheless, it may be worth exploring alternate dynamical initial conditions (e.g., initial turbulence) in future studies.

### 3.2. Day-Night Heat Redistribution

Several recent 1D radiative-transfer models include parameterizations of the day-night heat redistribution by the circulation (Burrows et al. 2006, 2007a). In these studies, an arbitrary fraction of the absorbed starlight is removed from the dayside and added to the nightside. To guide such efforts, we here quantify the magnitude of redistribution that occurs in our simulations. The goal is to obtain an equation for the mean nightside temperature and its modification by day-night advection. Starting with the thermodynamic energy equation (4), we express the advection terms in divergence form and invoke the continuity equation (3) to cancel out terms, yielding

$$\frac{\partial T}{\partial t} + \nabla \cdot (\mathbf{v}T) + \frac{\partial}{\partial p}(\omega T) = \frac{q}{c_p} + \frac{\omega}{\rho c_p}. \quad (7)$$

We then horizontally average the equation over the nightside hemisphere, yielding

$$\frac{\partial \langle T \rangle_{\text{night}}}{\partial t} = \left\langle \frac{q}{c_p} \right\rangle_{\text{night}} + \left\langle \frac{\omega}{\rho c_p} - \frac{\partial}{\partial p}(\omega T) \right\rangle_{\text{night}} - \langle \nabla \cdot (\mathbf{v}T) \rangle_{\text{night}}, \quad (8)$$

where  $\langle X \rangle_{\text{night}} \equiv (2\pi a^2)^{-1} \int X dA$ ,  $a$  is the planetary radius, the integral is taken over the nightside hemisphere (of area  $2\pi a^2$ ), and  $dA$  is the increment of horizontal area on the sphere. Using the divergence theorem, we can then rewrite  $\langle \nabla \cdot (\mathbf{v}T) \rangle_{\text{night}}$  as the product of the zonal (east-west) wind and temperature integrated along the day-night terminators:

$$\begin{aligned} \frac{\partial \langle T \rangle_{\text{night}}}{\partial t} = & \left\langle \frac{q}{c_p} \right\rangle_{\text{night}} + \left\langle \frac{\omega}{\rho c_p} - \frac{\partial}{\partial p}(\omega T) \right\rangle_{\text{night}} \\ & - \frac{1}{2\pi a} \int_{-90^\circ}^{90^\circ} u(\lambda_{\text{dawn}}, \phi, p) T(\lambda_{\text{dawn}}, \phi, p) d\phi \\ & + \frac{1}{2\pi a} \int_{-90^\circ}^{90^\circ} u(\lambda_{\text{dusk}}, \phi, p) T(\lambda_{\text{dusk}}, \phi, p) d\phi. \end{aligned} \quad (9)$$

Here,  $\lambda_{\text{dawn}}$  and  $\lambda_{\text{dusk}}$  refer to the longitudes of the “dawn” and “dusk” terminators ( $-90^\circ$  and  $90^\circ$ ), and we have used the fact that for zero obliquity the terminators lie at constant longitude.

Equation (9) provides a framework for quantifying the day-night heat redistribution. On the right-hand side, the first and second terms in brackets are the temperature change due to radiative heating/cooling and vertical motion, respectively. The final two terms are the “heat source” associated with thermal-energy transport from dayside to nightside. Burrows et al. (2006, 2007a) took the approach of introducing an ad hoc parameterization for the third and fourth terms on the right-hand side of equation (9). Here, we explicitly calculate these terms from our simulations.

Figure 10 shows these heat transports versus pressure for our nominal HD 189733b simulation. The dashed and dotted curves show the transport across the terminators at longitude  $-90^\circ$  and  $+90^\circ$ , respectively, and the solid curve shows their sum. Several points deserve mention. First, the individual transports (*dashed and dotted curves*) are large at low pressure and decay toward zero at pressures  $>100$  bars, which results from the fact that, in these simulations, the circulation is strong aloft and dies out with depth.

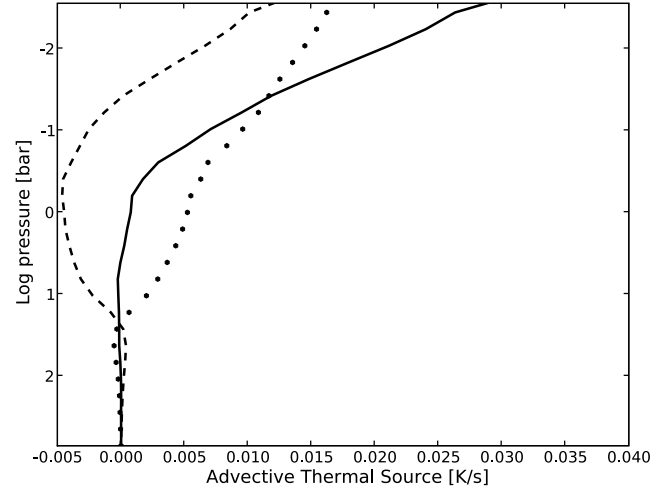


FIG. 10.—Heat source, expressed in  $\text{K s}^{-1}$ , associated with day-to-night horizontal advection across the terminators for our nominal HD 189733b simulation. Dashed and dotted lines show heat transport across the dawn and dusk terminators, respectively (third and fourth terms on the right-hand side of eq. [9]). The solid line shows their sum.

Second, these individual terms (Fig. 10, *dotted and dashed curves*) sum constructively at pressures  $<50$  mbar but have opposite signs at greater pressures. This results from the fact that, at low pressure, the circulation transports air from dayside to nightside across *both* terminators (see Figs. 4 and 5), leading to a positive heat source for the nightside across both terminators. In contrast, at depth, the superrotating equatorial jet transports air from the dayside to nightside across the dusk terminator (leading to a positive contribution in Fig. 10, *dotted curve*) but transports air from the nightside to dayside across the dawn terminator (leading to a negative contribution in Fig. 10, *dashed curve*). At the altitudes of the superrotating jet, the day-night heat transports across the two terminators largely cancel. As a result of these effects, the *net* advective heat source is almost zero at pressures exceeding  $\sim 1$  bar but becomes large at lower pressure (*solid curve*). The magnitudes reach  $\sim 0.02 \text{ K s}^{-1}$  near the top of the model.

The magnitude of the net advective heat source (Fig. 10, *solid curve*) increases monotonically with altitude. This differs from the scheme used by Burrows et al. (2007a, 2007b) to predict light curves and secondary-eclipse depths, which confined the heat transport to pressures between  $\sim 0.01$  and 0.1 bars. Our simulations suggest that a continuous, upward-increasing profile of temperature modification may be preferable.

Interestingly, pressures where the advective temperature modification is greatest (i.e., the top of the model) have the largest day-night temperature difference. The enormous radiative heating/cooling rates at these levels overwhelm the transport, allowing near-radiative-equilibrium conditions (with large day-night temperature differences) to be maintained. In contrast, at deeper levels, the transport modifies the temperature more weakly, but the heating/cooling rates are low, allowing relatively homogenized day-night temperatures to be maintained. This situation belies simple descriptions (common in the literature) of planets with large day-night temperature differences having “inefficient” redistribution and those with homogenized conditions as having “efficient” redistribution.

## 4. SPECTRA AND LIGHT CURVES

We calculate spectra and light curves from our simulations following the methods described in Fortney et al. (2006a). The 3D

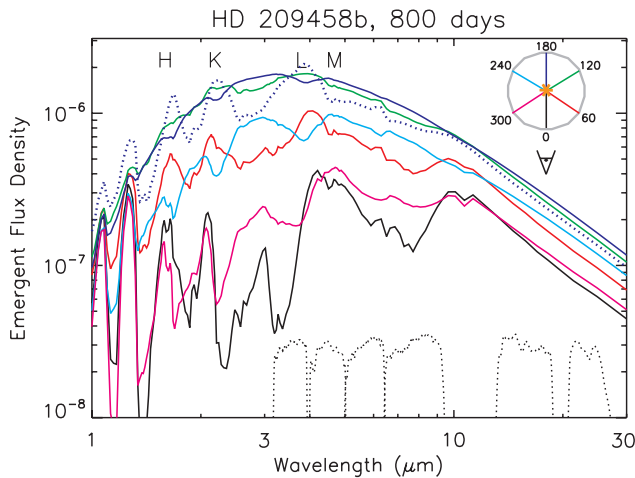


FIG. 11.—Emergent flux density ( $\text{ergs s}^{-1} \text{cm}^{-2} \text{Hz}^{-1}$ ) from the nominal HD 209458b simulation at six phases, assuming equilibrium chemistry: night-side, as seen during transit, *black*;  $60^\circ$  after transit, *red*;  $120^\circ$  after transit, *green*; dayside, as seen during secondary eclipse, *dark blue*;  $60^\circ$  after secondary eclipse, *light blue*; and  $120^\circ$  after secondary eclipse, *magenta*. The key in the top right corner is color-coded with the spectra to illustrate the sequence. For reference, the dotted blue curve shows the spectrum of a 1D, global-average radiative-equilibrium model atmosphere assuming all the starlight is evenly distributed over the full  $4\pi$  sr of the planet; it assumes chemical equilibrium, adopts solar metallicity (incorporating rain-out where relevant), and is cloud free. Thin dotted black lines at the bottom of the figure show normalized *Spitzer* bandpasses and the letters at the top show locations of the *H*, *K*, *L*, and *M* bands.

temperature field from a dynamical simulation at a given time can be viewed as numerous individual  $T(p)$  columns, one for each (longitude, latitude) location on the grid. Our low- and high-resolution simulations contain 3240 and 12,960 such columns, respectively. At any orbital phase (except during secondary eclipse), half of these columns will be visible from Earth. Assuming solar metallicity, we run each such profile through our radiative-transfer solver (§ 2.2) to determine the net emergent flux density versus wavelength for that column. This calculation properly includes the appropriate value of  $\mu_\oplus$  for each column, where  $\mu_\oplus$  is the cosine of the angle between local vertical of each column and the line of sight to Earth; this naturally accounts for any limb brightening or darkening. The emergent flux calculated for each column is then weighted by the apparent area of that patch of the planet as viewed from Earth; these are then summed to obtain the total emergent flux density of the planet at a given orbital phase. Fortney et al. (2006a) gives further details on the method.

Figure 11 depicts the resulting spectra for our nominal HD 209458b case under the assumption that local chemical equilibrium holds; qualitatively similar behavior occurs for HD 189733b. The spectra vary strongly with orbital phase. During secondary eclipse (*black solid curves*), the emergent flux is low and deep absorption bands of  $\text{CH}_4$  and  $\text{H}_2\text{O}$  appear. Away from transit, as the dayside comes into view, the infrared flux increases and the absorption bands become shallower. Near secondary eclipse (*dark blue*), the dayside faces Earth and the spectra exhibit only modest deviations from a blackbody. Interestingly, at this phase, the weak spectral features that do exist have flipped into emission.

These phase variations in spectra result directly from the fact that the simulated  $T(p)$  structure depends strongly on longitude. The radiative time constant is short at low pressure and long at high pressure (Fig. 2). Thus, on the nightside, the air aloft cools more rapidly than the air at depth, leading to a temperature that decreases strongly with altitude (Fig. 6). Conversely, on the dayside, the air aloft warms more rapidly than the air at depth, leading

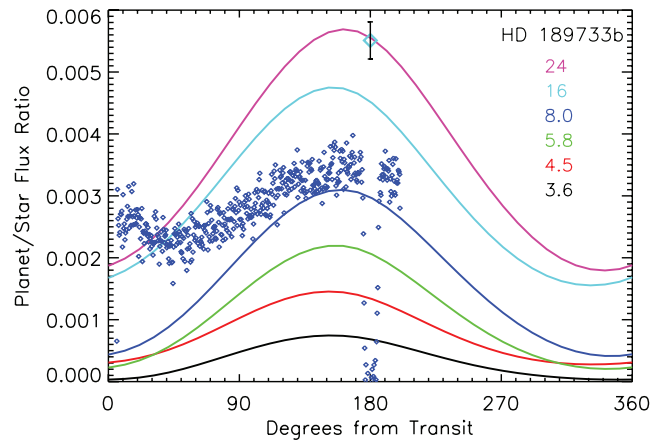


FIG. 12.—Light curves vs. orbital phase calculated in *Spitzer* bandpasses for HD 189733b. From top to bottom, the light curves are for wavelengths of  $24 \mu\text{m}$  (magenta),  $16 \mu\text{m}$  (light blue),  $8 \mu\text{m}$  (dark blue),  $5.8 \mu\text{m}$  (green),  $4.5 \mu\text{m}$  (red), and  $3.6 \mu\text{m}$  (black), respectively. Overplotted is the *Spitzer*  $8 \mu\text{m}$  light curve from Knutson et al. (2007) in dark blue and the  $16 \mu\text{m}$  secondary-eclipse depth from Deming et al. (2006) in light blue.

to a shallower structure that is quasi-isothermal or even exhibits a temperature inversion where  $T$  increases with altitude (Fig. 6). This latter behavior is the reason for the weak emission features in the dayside spectra (Fig. 11, *dark blue curves*).

We now turn to infrared light curves. Integrating our spectra and the Kurucz (1993) model of the star HD 189733 or HD 209458 (as appropriate) over the *Spitzer* bandpasses, we calculate the planet-to-star flux ratios versus orbital phase. Figures 12 and 13 display these light curves for equilibrium chemistry for our nominal models of HD 189733b and HD 209458b. As in Fortney et al. (2006a) the light curves here show a phase offset that results from the distortion of the temperature field by dynamics—most importantly, the eastward displacement of the hottest region from the substellar point and coldest region from the antistellar point, which causes the flux minima and maxima to occur before transit and secondary eclipse, respectively. The offset is greatest ( $\sim 30^\circ$ ) at  $3.6 \mu\text{m}$  and smallest ( $\sim 20^\circ$  for HD 189733b and  $13^\circ$  for HD 209458b) at  $24 \mu\text{m}$ . As described in Fortney et al. (2006a)

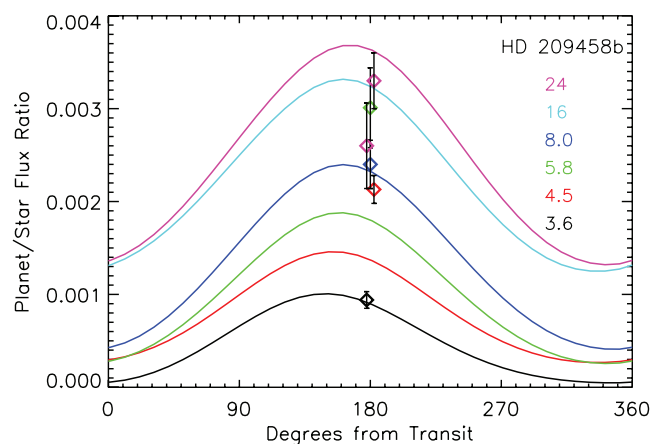


FIG. 13.—Same as in Fig. 12, but for HD 209458b. Diamonds give measured *Spitzer* secondary-eclipse depths with  $1\sigma$  error bars. Wavelengths of measurements and light curves are color coded to each other and to the numbers given in the plot. Magenta is  $24 \mu\text{m}$  (Deming et al. [2005] for the lower point, and D. Deming [2007, private communication] for the upper point), light blue is  $16 \mu\text{m}$ , dark blue is  $8 \mu\text{m}$  (Knutson et al. 2007), green is  $5.8 \mu\text{m}$ , red is  $4.5 \mu\text{m}$ , and black is  $3.6 \mu\text{m}$  (all from Knutson et al. 2008).

this wavelength-dependence results from the pressure-dependence of the photospheres, which tend to be at lower pressures for the longer *Spitzer* wavelengths. In our simulations, lower pressures have temperature patterns that more closely track the stellar heating patterns (Figs. 4 and 5), leading to the smaller phase shifts.

In our simulations, the infrared light curves reach a steady pattern relatively quickly. Light curves calculated at 100 days are very similar to those calculated at 900 days.

Figure 12 compares our light curves to the  $8\ \mu\text{m}$  *Spitzer* IRAC light curve of HD 189733b (Knutson et al. 2007). Interestingly, our simulations correctly produce the observed offset of the flux maximum from the time of secondary eclipse ( $16^\circ \pm 6^\circ$ ); however, we do not explain the location of the flux minimum, which occurs before transit in our simulations but after transit in the observations. To explain this feature would require a cold region to the west of the antistellar point. Because the low-latitude winds in our simulations are predominantly eastward, the cold region in our simulation is displaced to the east rather than the west. In the context of the simulations presented here, simultaneously explaining both an eastward displacement of the hot region and a westward displacement of the cold region is difficult.

If the circulation is quasi-steady, one possibility is that the dayside and nightside  $8\ \mu\text{m}$  photospheres sample different pressures; the observed light curve might be explained if the equatorial jet speed were eastward at the pressure of the dayside photosphere and westward at the pressure of the nightside photosphere. Another possibility is that a localized region of strong ascending motion (perhaps driven by absorption or breaking of atmospheric waves) could transport low-entropy (hence low-temperature) air to the photosphere level in a localized region, perhaps explaining the low-flux region. Alternatively, perhaps meandering hot and cold vortices could lead to time-variable temperature patterns and light curves (Cho et al. 2003; Rauscher et al. 2007a, 2007b); the low-flux region might then result from fortuitous placement of a cold vortex to the west of the antistellar point at the time of the observations. However, we caution that the star HD 189733 exhibits starspots that could influence the light curve; it is unclear whether all the structure in the light curve results from the planet rather than variability in the star. Future observational and theoretical work may resolve this ambiguity.

Perhaps more importantly, our simulations greatly underpredict the  $8\ \mu\text{m}$  flux on the planet's nightside (Fig. 12), suggesting that our nightside temperatures are too cold at the  $8\ \mu\text{m}$  photosphere. At the expected  $8\ \mu\text{m}$  photospheric pressure of  $\sim 30$  mbar, our radiative time constants vary from  $\sim 10^4$  s at 1500 K to  $10^5$  s at 500 K and rapidly rise to  $10^7$  s at temperatures less than 500 K (Fig. 2). For an equatorial jet speed of  $\sim 3\ \text{km s}^{-1}$  relevant for our simulations, the time to advect air parcels across a hemisphere is  $10^5$  s; thus, in our simulations, the nightside temperature at the  $8\ \mu\text{m}$  photosphere rapidly cools to  $\sim 500$  K, at which point further cooling is inhibited by the rapidly increasing  $\tau_{\text{rad}}$ . In contrast, the nightside  $8\ \mu\text{m}$  brightness temperature inferred from the Knutson et al. (2007) light curve is  $973 \pm 33$  K.

The fact that we overpredict the  $8\ \mu\text{m}$  day-night flux variation (and underpredict the absolute nightside flux) probably results from the simplifications inherent to the Newtonian heating/cooling scheme. Newtonian heating/cooling neglects the fact that the radiative equilibrium temperature and timescale can depend on the atmosphere's dynamical response, particularly when actual temperatures are far from radiative equilibrium. In reality, nonlinearities not included in the Newtonian relaxation framework can lead to radiative interactions between vertical levels that are not accounted for here. For example, because of the slow radiative heating rates at deep levels, the temperatures at  $p \geq 1$  bar become

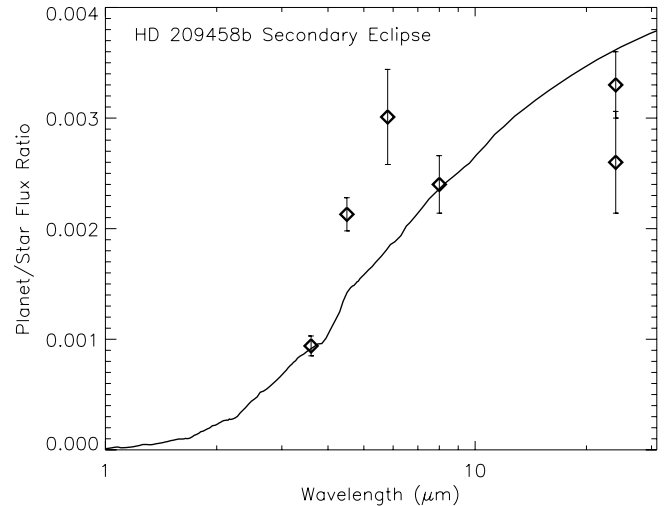


FIG. 14.—Planet-to-star flux ratio vs. wavelength for our nominal HD 209458b simulation at the time immediately before/after secondary eclipse. Points show measured secondary-eclipse depths (Deming et al. 2005; Knutson et al. 2007, 2008). As discussed in the text, our inability to fit the points at 4.5 and 5.8  $\mu\text{m}$  probably results from the lack of a stratosphere in our simulations.

homogenized between day- and nightsides; upwelling infrared radiation from this level will then warm the entire  $p$ - $T$  structure at  $p < 1$  bar and lead to nightside radiative-equilibrium temperatures that—because of this dynamical response—exceed those in Figure 1. This could lead to warmer nightside conditions than predicted here.

Next consider HD 209458b (Fig. 13). From several brief *Spitzer* observations at different phases, Cowan et al. (2007) place a  $2\ \sigma$  upper limit of 0.0015 on the peak-to-peak flux variation at  $8\ \mu\text{m}$ . In contrast, our light curve calculated under the assumption of equilibrium chemistry exhibits a peak-to-peak variation at  $8\ \mu\text{m}$  of  $\sim 0.0020$ , modestly higher than the upper limit. Regarding secondary-eclipse photometry, we match well the observed eclipse depths at 3.5 and  $8\ \mu\text{m}$  (Knutson et al. 2008). Two measurements exist of the  $24\ \mu\text{m}$  eclipse depth,  $0.0026 \pm 0.00046$  (Deming et al. 2005) and  $0.0033 \pm 0.0003$  (D. Deming 2007, private communication); our simulated light curve is marginally consistent with the latter. On the other hand, we underpredict the 4.5  $\mu\text{m}$  and 5.8  $\mu\text{m}$  eclipse depths by  $\sim 40\%$  (see also Fig. 14). The high flux at these wavelengths has been interpreted as resulting from a thermal inversion at pressures  $< 0.1$  bar (Knutson et al. 2008; Burrows et al. 2007b). Producing this feature may require the existence of stratospheric absorbers such as TiO and VO (Fortney et al. 2008; Burrows et al. 2007a, 2007b), which are not present in these models (see § 2.2).

Although in chemical equilibrium the primary carbon carrier would be CO on the dayside and  $\text{CH}_4$  on the nightside, Cooper & Showman (2006) showed that interconversion between CO and  $\text{CH}_4$  should become chemically quenched at low pressure, leading to nearly constant abundances of these species everywhere above the photosphere. For HD 209458b, their simulations suggested a quenched  $\text{CH}_4$  mole fraction corresponding to  $\sim 1\%$ – $2\%$  of the total carbon. Although Cooper & Showman (2006) did not consider HD 189733b specifically, their “cold” parameter variation has similar temperatures to our HD 189733b simulation; the quenched  $\text{CH}_4$  abundance was  $\sim 20\%$  of the total CO+ $\text{CH}_4$  in this case. The specific values should be viewed as quite uncertain.

We thus recalculated the phase-dependent spectra and light curves assuming constant CO and  $\text{CH}_4$  mole fractions rather than chemical equilibrium. Having only a fraction of the carbon

in CH<sub>4</sub> on the nightside (compared to the equilibrium case where 100% of the nightside carbon resides in CH<sub>4</sub>) lessens the depth of the nightside absorption features at 3.6 and 8 μm, making the nightside brighter at these wavelengths.<sup>10</sup> The effect is modest when the fraction of carbon in methane is 20% but strong when it is only 2%. In the latter case, the day-night flux variation at 3.6 μm is reduced from a factor of ~10 to ~2 while that at 8 μm is reduced from a factor of ~4 to ~2.5 (see Fortney et al. 2006a, Fig. 9).

By lessening the predicted day-night flux variation, this disequilibrium effect allows us to fit the upper limit of 0.0015 on the peak-to-peak planet/star flux variation of HD 209458b at 8 μm (Cowan et al. 2007). It could also potentially help provide a better fit to the 8 μm light curve of HD 189733b (Fig. 12; Knutson et al. 2007), but only if the planet's nightside methane abundance is relatively small (perhaps 5% or less of the total carbon if the metallicity is solar). Clearly, light curves in the 3.6 μm *Spitzer* band (and the 4.5 μm/3.6 μm band ratio, which is sensitive to the CH<sub>4</sub>/CO ratio) will provide important constraints on possible disequilibrium chemistry.

## 5. COMPARISON TO OTHER WORK

Showman et al. (2007) reviewed the various approaches adopted for investigating the atmospheric circulation of hot Jupiters; here we expand on key points.

Of the published models, Dobbs-Dixon & Lin (2008) most strongly resembles the approach taken here. They performed 3D numerical simulations of the Navier-Stokes equations in the low- and midlatitudes (excluding the poles). Radiation was parameterized by flux-limited diffusion using Rosseland-mean opacities. They parameterized stellar irradiation by imposing a spatially varying temperature at the upper boundary (hot on the dayside and cold on the nightside); downward diffusion of energy at the model top thus induces heating on the dayside while upward diffusion out the model top induces cooling on the nightside. Their nominal simulations adopt opacities relevant to interstellar-medium (ISM) gas and grains; as they point out, this is probably an overestimate for planetary atmospheres, where significant particle growth and settling is expected. They thus also performed cases with opacities reduced by factors of 100 and 1000 relative to the ISM and suggest that 100-fold reduction may be most appropriate for hot Jupiters.

For diffusion to be a good approximation, the mean-free path of the relevant photons must be much less than the length scales over which the atmospheric properties vary vertically. This is an excellent approximation in the deep interior where opacities are high. However, the diffusion approximation breaks down near the photosphere, where a large fraction of infrared photons can escape directly to space. This is the important region for infrared spectra, light curves, and secondary-eclipse depths. In this region, radiative fluxes cannot be represented as a diffusivity times the local temperature gradient, as postulated in the diffusion approach; instead, the radiative transfer involves nonlocal interactions between different atmospheric levels. Nevertheless, Dobbs-Dixon & Lin (2008)'s approach, like ours, serves its intended purpose of providing an approximate, computationally efficient means to force a plausible flow.

A further difference between Dobbs-Dixon & Lin (2008) and the present study involves the representation of dynamics. They solved the Navier-Stokes equations rather than the primitive equations; we return to this issue in § 6. In addition, they included the centrifugal acceleration in the equation of motion; this differs from

the approach taken in most planetary circulation models, which typically account for the gravitational relaxation of the planetary interior to the planetary rotation by absorbing the centrifugal force into the gravity.<sup>11</sup> At the present time, however, the greatest source of uncertainty lies in the treatment of radiation rather than dynamics.

Despite the differences between Dobbs-Dixon & Lin (2008)'s approach and that adopted here, their basic results share strong similarities with ours. Because their case exploring opacities 100 times less than ISM values seems most relevant to hot Jupiters (Dobbs-Dixon & Lin 2008), this is their best simulation to compare with ours. In agreement with our results, this case develops a banded pattern at the photosphere with a broad, planet-encircling superrotating equatorial jet reaching speeds of 3 km s<sup>-1</sup> and weaker (~1–2 km s<sup>-1</sup>) westward jets in the midlatitudes (see their Figs. 9 and 10, *top panels*). Their day-night temperature differences at the photosphere reach ~500 K. Although our simulated day-night temperature difference at the photosphere differs somewhat from theirs (~800 and ~300 K for our nominal and 10 × nominal τ<sub>rad</sub> cases, respectively), the qualitative similarities between their simulation and ours are striking given the distinct approaches.<sup>12</sup> These similarities, which lend credence to both approaches, are encouraging because they suggest that the basic flow regime on hot Jupiters is relatively insensitive to differences in model formulation.

Langton & Laughlin (2007) performed numerical simulations of the atmospheric flow on hot Jupiters using the one-layer shallow-water equations, which govern the behavior of a thin layer of hydrostatically balanced, constant-density fluid on a sphere. The momentum and continuity equations are (e.g., Pedlosky 1987, chap. 3)

$$\frac{d\mathbf{v}}{dt} = -g\nabla h - f\mathbf{k} \times \mathbf{v}, \quad (10)$$

$$\frac{\partial h}{\partial t} = -\nabla \cdot (h\mathbf{v}), \quad (11)$$

where  $\mathbf{v}(\lambda, \phi, t)$  is horizontal velocity,  $h(\lambda, \phi, t)$  is the thickness of the fluid layer, and  $g$  is gravity. Note that, because of the constant-density assumption, the temperature is undefined and there is no thermodynamic-energy equation. When writing these equations, Langton & Laughlin (2007) replaced  $gh$  with  $RT$ , causing the continuity equation (eq. [11]) to resemble an energy equation. This is not a valid procedure, however, since the shallow-water layer thickness is a representation of mass per area between two bounding material surfaces and is thus a distinct quantity from temperature<sup>13</sup>; as mentioned above, the constant-density assumption prevents temperature from entering the shallow-water system. Their temperature fields are therefore best interpreted as shallow-water

<sup>11</sup> For example, a hypothetical rotating planet with no radiative forcing, no initial horizontal temperature/pressure gradients (i.e., along the rotationally modified equipotentials), and zero initial winds should remain motionless over time. If the initial condition is spherically symmetric, as assumed by Dobbs-Dixon & Lin (2008), then inclusion of the centrifugal acceleration, however, would cause equatorward motion in such a case — effectively forcing the equatorial bulge to develop in the modeled thin atmosphere rather than throughout the planetary interior.

<sup>12</sup> Their cases using ISM opacities exhibit some qualitative differences in jet structure relative to both their reduced-opacity cases and our results. These differences presumably result from the extreme opacity in these simulations.

<sup>13</sup> Equating  $gh$  to  $RT$  is equivalent to assuming  $h = RT/g$ , which is just the atmospheric pressure scale height derived for a compressible ideal-gas equation of state. This is incompatible with the incompressibility assumption on which shallow water is based; furthermore, a scale height is defined as the height between two isobars whereas the shallow-water layer thickness is the height between two surfaces of constant potential-density (e.g., density in the ocean and entropy in the atmosphere).

<sup>10</sup> In our simulations, the dayside fluxes are less sensitive to the CH<sub>4</sub>/CO ratio because of the near-isothermal dayside conditions.

layer thickness. Langton & Laughlin (2007) forced equation (11) using a Newtonian-relaxation scheme that adds mass on the day-side and removes it on the nightside, which is intended as a simple means to represent dayside radiative heating and nightside cooling. Their simulations exhibit development of winds reaching  $\sim 1 \text{ km s}^{-1}$ .

In a subsequent study, Langton & Laughlin (2008) performed global, 2D hydrodynamic simulations of the flow on hot Jupiters with eccentric orbits. This system of equations, unlike the shallow-water set, contains independent continuity and energy equations; governing variables are  $\mathbf{v}$ ,  $\rho$ , and  $T$  over the globe. They treated radiation using a two-band model, one for stellar irradiation and the other for planetary thermal radiation under the assumption that the local emission occurs as a blackbody. Their simulations develop strong lateral temperature gradients as one side of the planet is flash heated during periastron passage; this leads to complex and highly turbulent flow fields as the resulting vortex structures become dynamically unstable. This natural development of turbulence from the hemispheric-scale stellar forcing is an interesting result that has not occurred to date in models of hot Jupiters with zero eccentricity (Showman & Guillot 2002; Cooper & Showman 2005, 2006; Langton & Laughlin 2007; Dobbs-Dixon & Lin 2008), and it may have important implications for infrared light curves (Langton & Laughlin 2008). Nevertheless, 2D dynamics differs in important ways from 3D dynamics, and it has not yet been demonstrated whether this type of 2D model can reproduce the known flow fields on solar-system planets, which is an important benchmark for any model. Exploring 3D circulation models of hot Jupiters on eccentric orbits is clearly an interesting avenue for future research.

Cho et al. (2003, 2008) performed global one-layer simulations of the flow on hot Jupiters using the equivalent-barotropic equations, which are essentially a vertically averaged version of the 3D primitive equations. A major difference with the other studies described here is that Cho et al. (2003, 2008) did not include any radiative heating/cooling; instead, they forced their flows using a combination of small-scale turbulence in the initial condition and a hemispheric-scale pressure deflection intended to qualitatively represent the dynamical effects of the day-night heating gradient. In cases when strong initial turbulence was included, their flows developed meandering polar vortices, waves, and a high degree of turbulent mixing. The turbulent initial condition that enables these outcomes was intended as a parameterization of turbulence generation by atmospheric instabilities. Although all planetary atmospheres are turbulent, the appropriate turbulent length scales and energetic amplitudes remain unknown for hot Jupiters, and may well vary from planet to planet. If such turbulence is indeed present at the levels explored by Cho et al., it should ideally develop naturally in models that force the flow (for example with radiative heating/cooling). So far, however, radiatively forced investigations of hot Jupiters in circular orbits have exhibited relatively steady circulation patterns that lack the degree of turbulent variability seen in the Cho et al. simulations (Showman & Guillot 2002; Cooper & Showman 2005; Langton & Laughlin 2007; Dobbs-Dixon & Lin 2008 and the present study), with the notable exception of Langton & Laughlin (2008)'s 2D study of hot Jupiters in highly eccentric orbits. It will be interesting to see if this continues to be the case as a wider range of hot Jupiters is explored and model resolutions and forcing realism improve over time.

In contrast to the above dynamical models, Iro et al. (2005) and Burrows et al. (2006, 2007a, 2007b) explored models of hot Jupiters that used realistic radiative-transfer schemes but made

ad hoc assumptions for the effect of dynamics on the thermal budget. Iro et al. (2005) assumed atmospheric winds that correspond to solid-body rotation; the speed at the equator was a free parameter varied from  $0.5$  to  $2 \text{ km s}^{-1}$ . Burrows et al. (2006, 2007b, 2007a) simply removed an arbitrary fraction of the stellar irradiation from the dayside and placed it on the nightside to mimic the effect of atmospheric winds. This is a novel approach that allows the exploration of how (for example) day-night temperature differences should depend on the day-night heat transport. As these authors are careful to point out, however, it is not a rigorous treatment of dynamics.

## 6. COMMENTS ON HYDROSTATIC BALANCE AND VERTICAL MOTIONS

### 6.1. *The Validity of Hydrostatic Balance*

A scaling analysis demonstrates that local hydrostatic balance is approximately valid for the large-scale flow on hot Jupiters (Showman et al. 2007); we reiterate the arguments here. It is important to emphasize that the local-hydrostatic-balance assumption in the primitive equations derives from the assumption of large aspect ratio and *not* from any assumption on wind speed. However, the fact that estimated wind speeds on hot Jupiters are several  $\text{km s}^{-1}$ , which is close to the  $3 \text{ km s}^{-1}$  speed of sound in these atmospheres, suggests that we consider the validity of the primitive equations in the hot-Jupiter context. The full Navier-Stokes vertical momentum equation can be written

$$\frac{\partial w}{\partial t} + \mathbf{v} \cdot \nabla w = -\frac{1}{\rho} \frac{\partial p}{\partial z} - g + 2u\Omega \cos \phi, \quad (12)$$

where  $w$  is vertical wind speed,  $t$  is time,  $\mathbf{v}$  is the horizontal wind velocity, and  $u$  is the east-west wind speed. The background static hydrostatic balance is irrelevant to atmospheric circulation and can be removed from the equation. Define  $p = p_0(z) + p'$  and  $\rho = \rho_0(z) + \rho'$ , where  $p_0$  and  $\rho_0$  are the time-independent basic-state pressure and density and, by construction,  $\partial p_0 / \partial z \equiv -\rho_0 g$ . Primed quantities are the deviations from this basic state caused by dynamics. Substituting these expressions into equation (12), we can rewrite the equation as

$$\frac{\partial w}{\partial t} + \mathbf{v} \cdot \nabla w = -\frac{1}{\rho} \left( \frac{\partial p'}{\partial z} - \rho' g \right) + 2u\Omega \cos \phi, \quad (13)$$

where the basic-state hydrostatic balanced has been subtracted off. The terms in parentheses give only the flow-induced contributions to vertical pressure gradient and weight (they go to zero in a static atmosphere).

For local hydrostatic balance to be a reasonable approximation, the terms in parenthesis must be much larger than the other terms in the equation. The magnitude of  $\partial w / \partial t$  is approximately  $w / \tau$ , where  $\tau$  is a flow evolution timescale, and the magnitude of  $\mathbf{v} \cdot \nabla w$  is the greater of  $uw/L$  and  $w^2/H$ , where  $L$  is the horizontal flow scale and  $H$  is the vertical flow scale. For global-scale flows,  $L \sim 10^7 - 10^8 \text{ m}$ , and  $\tau$  (for example estimated using an advective time  $L/u$ ) is  $\sim 10^4 - 10^5 \text{ s}$ . The large-scale flow varies vertically over a scale height  $H \sim 300 \text{ km}$  (Showman & Guillot 2002; Cooper & Showman 2005, 2006; Dobbs-Dixon & Lin 2008). For the simulated flow regime in Cooper & Showman (2005, 2006) and Dobbs-Dixon & Lin (2008)  $\mathbf{v} \sim u \sim 3 \text{ km s}^{-1}$ ,  $g \sim 10 \text{ m s}^{-2}$ ,  $\Omega \sim 2 \times 10^{-5} \text{ s}^{-1}$ , and  $w \sim 10 - 100 \text{ m s}^{-1}$ . With these values, we find that  $\partial w / \partial t \leq 10^{-2} \text{ m s}^{-2}$ ,  $uw/L \leq 0.03 \text{ m s}^{-2}$ ,  $w^2/H \leq 0.03 \text{ m s}^{-2}$ , and  $\Omega u \sim 0.1 \text{ m s}^{-2}$ . In comparison, for a hot Jupiter with day-night temperature differences of several hundred K,

the flow-induced hydrostatic terms  $\rho'g/\rho$  and  $\rho^{-1}\partial p'/\partial z$  are each  $\sim 10 \text{ m s}^{-2}$ .

This analysis implies that, for global-scale hot-Jupiter flows at the atmospheric pressures considered in our model ( $p > 1 \text{ mbar}$ ), the greatest departure from hydrostaticity results from the vertical Coriolis force, which causes a  $\sim 1\%$  deviation from hydrostatic balance. The acceleration terms on the left side of equation (13) (which are necessary for vertically propagating sound waves) cause a  $\sim 0.3\%$  deviation from hydrostatic balance. Hydrostatic balance is thus a reasonable approximation for the large-scale flow. Nonhydrostatic effects of course become important at small scales, and it is conceivable that these effects interact with the large-scale flow in nontrivial ways. For hot Jupiters, the acceleration terms on the left side of equation (13) only become important for structures with vertical or horizontal scales less than  $\sim 30 \text{ km}$  and  $\sim 500\text{--}1000 \text{ km}$ , respectively. In a numerical model that solved the full Navier-Stokes equations, the grid resolution would have to be substantially finer than these values for the nonhydrostatic behavior to be accurately represented. A full Navier-Stokes solution with a coarse resolution would effectively be resolving just the global-scale hydrostatic component of the flow.

Despite the above, some hot Jupiters may be losing mass from the top of their atmospheres (Vidal-Madjar et al. 2003, 2004), which suggests that hydrostatic equilibrium should break down at extremely low pressures (above the top of our model) where this outflow occurs.

### 6.2. Vertical Velocities

We wish here to clarify the issue of vertical velocities. Dobbs-Dixon & Lin (2008) suggested that vertical motions are faster in the full Navier-Stokes system than in the primitive equations because of the different vertical momentum equations in these systems. Certainly, velocities in a convection zone require use of a momentum equation that includes vertical accelerations. However, in statically stable atmospheres, the primary control over the vertical velocity in a quasi-steady overturning circulation (relevant to the regime simulated here) is *not* the vertical momentum equation but the thermodynamic energy equation (eq. [4]). The reason is that, in this situation, the radiative heating/cooling rate controls the speed of vertical motion. Because entropy increases with height in a statically stable atmosphere, adiabatic expansion/contraction in ascending (descending) air causes temperature at a given height to decrease (increase) over time. In the absence of radiation, such steady flow patterns are unsustainable because they induce density perturbations that resist the motion (i.e., ascending air becomes denser and descending air becomes less dense than the surroundings at that altitude). Thus, steady vertical motion in a stable atmosphere can only occur as fast as radiation can remove the temperature perturbations caused by the adiabatic ascent/descent. This provides a fundamental constraint on vertical motion that applies equally to the primitive and the Navier-Stokes equations.

To quantify this idea, consider equation (4), which can be written

$$\frac{\partial T}{\partial t} + \mathbf{v} \cdot \nabla T - \omega \frac{H^2 N^2}{R p} = \frac{q}{c_p}, \quad (14)$$

where  $H$  is the vertical scale height and  $N$  is the Brunt-Väisälä frequency (the oscillation frequency for a vertically displaced air parcel in a statically stable atmosphere). An upper limit on the attainable vertical velocity in a quasi-steady circulation in a statically stable atmosphere results from equating the right-hand side to the

third term on the left side. One then obtains a peak vertical velocity (measured in  $\text{Pa s}^{-1}$ )

$$\omega \sim \frac{q}{c_p} \frac{R p}{H^2 N^2}, \quad (15)$$

which can be approximately expressed as a peak vertical velocity in  $\text{m s}^{-1}$

$$w \sim \frac{q}{c_p} \frac{R}{H N^2}. \quad (16)$$

The equation of course couples to the rest of the dynamics via  $N^2$  and  $q/c_p$ . For hot Jupiter photospheres, where  $q/c_p \sim 10^{-2} \text{ K s}^{-1}$ ,  $H \sim 300 \text{ km}$ , and  $N \sim 0.001\text{--}0.01 \text{ s}^{-1}$  depending on temperature, gravity, and thermal gradient, we then expect  $w \sim 10\text{--}100 \text{ m s}^{-1}$  or less (Showman & Guillot 2002). Importantly, equation (16) makes no assumption about the form of the vertical momentum equation (hydrostatic versus Navier-Stokes); only quasi-steady flow and a statically stable atmosphere were invoked. Within the context of the static stabilities and heating rates assumed above, these vertical velocities should therefore apply to statically stable atmospheres regardless of whether they are modeled with the primitive or Navier-Stokes equations. On the other hand, because of the intense nightside cooling, some hot Jupiters may develop convection zones near the photosphere on the nightside. The primitive equations cannot capture the small-scale convective vertical velocities in this situation. Nevertheless, our simulations of HD 209458b and HD 189733b appear not to predict such detached convection regions.

## 7. CONCLUSIONS

We presented three-dimensional numerical simulations of the atmospheric circulation on HD 209458b and HD 189733b; calculated infrared spectra and light curves from the simulated temperature patterns; and compared these observables with available measurements. The simulations were forced with a simplified Newtonian heating/cooling scheme. Within the context of this approach, we have improved on earlier work by calculating for use in this scheme the true radiative-equilibrium temperatures as a function of longitude, latitude, and pressure; likewise, we calculated the radiative time constants as a function of both temperature and pressure over the 3D grid. These radiative time constants are generally consistent with earlier estimates (Iro et al. 2005) but span a much greater range of pressure and especially temperature.

In our simulations, HD 209458b and HD 189733b develop similar circulation patterns, although the latter has a global-average temperature  $\sim 200\text{--}300 \text{ K}$  cooler than the former (a result of the lower stellar flux). Consistent with earlier work (Cooper & Showman 2005, 2006), our simulations show that, at low pressure ( $< 10 \text{ mbar}$ ), the circulation transports air from dayside to nightside, both along the equator and over the poles. At high pressure ( $> 100 \text{ mbar}$ ), a banded structure emerges with a broad, fast ( $3\text{--}4 \text{ km s}^{-1}$ ) eastward equatorial jet flanked by weaker westward flow at high latitudes. The day-night temperature difference varies strongly with height and reaches  $500\text{--}1000 \text{ K}$  above the photosphere. Near the photosphere, the dynamics distorts the temperature pattern in a complex manner; consistent with our earlier work, this generally includes an eastward displacement of the hottest regions from the substellar point. Importantly, dynamics also pushes the vertical temperature profile  $T(p)$  far from radiative-equilibrium. The temperature decreases strongly with altitude on the nightside but becomes quasi-isothermal, or even exhibits an inversion layer, on the dayside.

Our calculated spectra, calculated assuming a cloud-free atmosphere with solar metallicity (appropriately modified for rainout) show that the nightside should exhibit deep absorption bands. On the dayside, however, the deviations of the spectrum from a blackbody become modest due to the quasi-isothermal structure. Nevertheless, in some simulations this dayside structure contains weak *emission* features, which result from the existence of a thermal inversion in these simulations.

Our light curves calculated in *Spitzer* bandpasses show that, for HD 189733b, we correctly explain the phase offset of the flux peak that occurs before the secondary eclipse measured in the 8  $\mu\text{m}$  light curve of Knutson et al. (2007) but we fail to explain the flux minimum that occurs after transit and we overpredict the total flux variation. For HD 209458b, we match the *Spitzer* IRAC 3.6 and 8  $\mu\text{m}$  secondary-eclipse depths, and marginally fit the latter of two 24  $\mu\text{m}$  MIPS measurements, but we underpredict the 4.5 and 5.8  $\mu\text{m}$  IRAC secondary-eclipse depths. This probably results from the lack of a strong stratosphere that seems to be implied by these observations. Future simulations that include a realistic representation of radiative transfer, including the possibility of TiO and VO opacity for the case of HD 209458b, may be needed to better fit these diverse observations.

Finally, we presented a scaling analysis suggesting that the large-scale ( $\geq 10^7$  m) flow on the hot Jupiters explored here should

be close to local hydrostatic balance; on these large scales, deviations from hydrostaticity are small. This result lends support to the primitive-equation approach adopted here. At the present time, the primary source of uncertainty is not the dynamical scheme but the representation of the forcing that drives the flow.

So far, all published studies of the circulation on hot Jupiters have forced the flow using relatively severe approximations to the radiative transfer or excluded heating/cooling entirely. Inclusion of realistic radiative transfer is an important goal for future work. Other areas for improvement include considering cloud/haze formation, alternate compositions (supersolar metallicity and the possibility of TiO and VO), and exploring a wider range of planetary parameters to capture the diversity of the growing number of known hot Jupiters.

This research was supported by NASA Planetary Atmospheres grants NNX07AF35G and NNG06GF28G and NASA GSRP NGT5-50462 to A. P. S. C. S. S. was supported in part by an appointment to the NASA Postdoctoral Program at the Astrobiology Institute at the University of Arizona, administered by Oak Ridge Associated Universities through a contract with NASA. M. S. M. acknowledges support from the NASA Office of Space Sciences.

## REFERENCES

- Arakawa, A., & Lamb, V. 1977, *Methods Comput. Phys.*, 17, 173  
 Barman, T. 2007, *ApJ*, 661, L191  
 Barman, T. S., Hauschildt, P. H., & Allard, F. 2005, *ApJ*, 632, 1132  
 Basu, S., Wilson, J., Richardson, M., & Ingersoll, A. P. 2006, *J. Geophys. Res.*, 111, 0900  
 Burrows, A., Budaj, J., & Hubeny, I. 2007a, *ApJ*, 661, 502  
 Burrows, A., Hubeny, I., Budaj, J., Knutson, H. A., & Charbonneau, D. 2007b, *ApJ*, 668, L171  
 Burrows, A., Sudarsky, D., & Hubeny, I. 2006, *ApJ*, 650, 1140  
 Burrows, A., et al. 1997, *ApJ*, 491, 856  
 Charbonneau, D., Brown, T. M., Burrows, A., & Laughlin, G. 2007, in *Protostars and Planets V*, ed. B. Reipurth, D. Jewitt, & K. Keil (Tucson: Univ. Arizona Press), 701  
 Charbonneau, D., Brown, T. M., Noyes, R. W., & Gilliland, R. L. 2002, *ApJ*, 568, 377  
 Cho, J. Y.-K., Menou, K., Hansen, B. M. S., & Seager, S. 2003, *ApJ*, 587, L117  
 ———. 2008, *ApJ*, 675, 817  
 Cho, J. Y.-K., & Polvani, L. M. 1996, *Science*, 8, 1531  
 Cooper, C. S., & Showman, A. P. 2005, *ApJ*, 629, L45  
 ———. 2006, *ApJ*, 649, 1048  
 Cowan, N. B., Agol, E., & Charbonneau, D. 2007, *MNRAS*, 379, 641  
 Deming, D., Harrington, J., Seager, S., & Richardson, L. J. 2006, *ApJ*, 644, 560  
 Deming, D., Seager, S., Richardson, L. J., & Harrington, J. 2005, *Nature*, 434, 740  
 Dobbs-Dixon, I., & Lin, D. N. C. 2008, *ApJ*, 673, 513  
 Forget, F., Hourdin, F., Fournier, R., Hourdin, C., Talagrand, O., Collins, M., Lewis, S. R., Read, P. L., & Huot, J.-P. 1999, *J. Geophys. Res.*, 104, 24155  
 Fortney, J. J., Cooper, C. S., Showman, A. P., Marley, M. S., & Freedman, R. S. 2006a, *ApJ*, 652, 746  
 Fortney, J. J., Lodders, K., Marley, M. S., & Freedman, R. S. 2008, *ApJ*, 678, 1419  
 Fortney, J. J., & Marley, M. S. 2007, *ApJ*, 666, L45  
 Fortney, J. J., Marley, M. S., Lodders, K., Saumon, D., & Freedman, R. 2005, *ApJ*, 627, L69  
 Fortney, J. J., Saumon, D., Marley, M. S., Lodders, K., & Freedman, R. S. 2006b, *ApJ*, 642, 495  
 Freedman, R. S., Marley, M. S., & Lodders, K. 2008, *ApJS*, 174, 504  
 Grillmair, C. J., Charbonneau, D., Burrows, A., Armus, L., Stauffer, J., Meadows, V., Van Cleve, J., & Levine, D. 2007, *ApJ*, 658, L115  
 Guillot, T., Burrows, A., Hubbard, W. B., Lunine, J. I., & Saumon, D. 1996, *ApJ*, 459, L35  
 Haberle, R. M., Houben, H., Barnes, J. R., & Young, R. E. 1997, *J. Geophys. Res.*, 102, 9051  
 Haberle, R. M., Murphy, J. R., & Schaeffer, J. 2003, *Icarus*, 161, 66  
 Haberle, R. M., Pollack, J. B., Barnes, J. R., Zurek, R. W., Leovy, C. B., Murphy, J. R., Lee, H., & Schaeffer, J. 1993, *J. Geophys. Res.*, 98, 3093  
 Harrington, J., Hansen, B. M., Luszcz, S. H., Seager, S., Deming, D., Menou, K., Cho, J. Y.-K., & Richardson, L. J. 2006, *Science*, 314, 623  
 Held, I. M., & Suarez, M. J. 1994, *Bull. Am. Meteorological Soc.*, 75, 1825  
 Herrstein, A., & Dowling, T. E. 2007, *J. Geophys. Res.*, 112, 04S08  
 Holton, J. R. 2004, *An Introduction to Dynamic Meteorology* (4th ed.; San Diego: Academic)  
 Houben, H., Haberle, R. M., Young, R. E., & Zent, A. P. 1997, *J. Geophys. Res.*, 102, 9069  
 Hourdin, F., Talagrand, O., Sadourny, R., Courtin, R., Gautier, D., & McKay, C. P. 1995, *Icarus*, 117, 358  
 Hubeny, I., Burrows, A., & Sudarsky, D. 2003, *ApJ*, 594, 1011  
 Iro, N., Bézard, B., & Guillot, T. 2005, *A&A*, 436, 719  
 Kalnay, E. 2003, *Atmospheric Modeling, Data Assimilation, and Predictability* (Cambridge: Cambridge Univ. Press)  
 Knutson, H. A., Charbonneau, D., Allen, L. E., Burrows, A., & Megeath, S. T. 2008, *ApJ*, 673, 526  
 Knutson, H. A., et al. 2007, *Nature*, 447, 183  
 Kurucz, R. 1993, Kurucz CD-ROM 13, ATLAS9 Stellar Atmosphere Programs and 2 km/s grid (Cambridge: SAO), 13  
 Langton, J., & Laughlin, G. 2007, *ApJ*, 657, L113  
 ———. 2008, *ApJ*, 674, 1106  
 Lee, C., Lewis, S. R., & Read, P. L. 2007, *J. Geophys. Res.*, 112, 04S11  
 Lian, Y., & Showman, A. P. 2008, *Icarus*, 194, 597  
 Lodders, K., & Fegley, B. 2002, *Icarus*, 155, 393  
 Lodders, K., & Fegley, Jr., B. 2006, in *Astrophysics Update*, Vol. 2, ed. J. W. Mason (Chichester: Praxis)  
 Marley, M. S., Gelino, C., Stephens, D., Lunine, J. I., & Freedman, R. 1999, *ApJ*, 513, 879  
 Marley, M. S., & McKay, C. P. 1999, *Icarus*, 138, 268  
 Marley, M. S., Saumon, D., Guillot, T., Freedman, R. S., Hubbard, W. B., Burrows, A., & Lunine, J. I. 1996, *Science*, 272, 1919  
 McKay, C. P., Pollack, J. B., & Courtin, R. 1989, *Icarus*, 80, 23  
 Menou, K., Cho, J. Y.-K., Seager, S., & Hansen, B. M. S. 2003, *ApJ*, 587, L113  
 Newman, C. E., Lewis, S. R., Read, P. L., & Forget, F. 2002, *J. Geophys. Res.*, 107, 5123  
 Pedlosky, J. 1987, *Geophysical Fluid Dynamics* (2nd ed.; New York: Springer)  
 Polvani, L. M., Waugh, D. W., & Plumb, R. A. 1995, *J. Atmos. Sci.*, 52, 1288  
 Rauscher, E., Menou, K., Cho, J. Y.-K., Seager, S., & Hansen, B. M. S. 2007a, *ApJ*, 662, L115  
 ———. 2007b, preprint (arXiv: 0712.2242R)  
 Redfield, S., Endl, M., Cochran, W. D., & Koesterke, L. 2008, *ApJ*, 673, L87  
 Richardson, L. J., Deming, D., Horning, K., Seager, S., & Harrington, J. 2007, *Nature*, 445, 892  
 Richardson, L. J., Deming, D., & Seager, S. 2003, *ApJ*, 597, 581  
 Saumon, D., & Guillot, T. 2004, *ApJ*, 609, 1170  
 Shapiro, R. 1970, *Rev. Geophys. Space Phys.*, 8, 359

- Showman, A. P. 2007, *J. Atmos. Sci.*, 64, 3132
- Showman, A. P., & Guillot, T. 2002, *A&A*, 385, 166
- Showman, A. P., Menou, K., & Y-K. Cho, J. 2007, preprint (arXiv: 0710.2930S)
- Suarez, M. J., & Takacs, L. L., ed. 1995, Documentation of the ARIES/GEOS Dynamical Core, ver. 2 (NASA Tech. Memo. 104606)
- Swain, M. R., Bouwman, J., Akeson, R., Lawler, S., & Beichman, C. 2008, *ApJ*, 674, 482
- Tinetti, G., et al. 2007, *Nature*, 448, 169
- Tokano, T., Neubauer, F. M., Laube, M., & McKay, C. P. 2001, *Icarus*, 153, 130
- Vasavada, A. R., & Showman, A. P. 2005, *Rep. Prog. Phys.*, 68, 1935
- Vidal-Madjar, A., Lecavelier des Etangs, A., Désert, J.-M., Ballester, G. E., Ferlet, R., Hébrard, G., & Mayor, M. 2003, *Nature*, 422, 143
- . 2004, *ApJ*, 604, L69
- Williams, G. P. 2003, *J. Atmos. Sci.*, 60, 1270
- Yamamoto, M., & Takahashi, M. 2003, *J. Atmos. Sci.*, 60, 561
- . 2006, *J. Atmos. Sci.*, 63, 3296